Journal of Geodesy (2025) 99:34
https://doi.org/10.1007/s00190-025-01958-2

ORIGINAL ARTICLE

Accurate computation of gravitational curvature of a tesseroid

Xiao-Le Deng[1]

Received: 14 March 2024 / Accepted: 26 March 2025 / Published online: 29 April 2025

Abstract

In recent years, the fundamental quantity of the gravitational field has been extended from gravitational potential, gravitational vector, and gravitational gradient tensor to gravitational curvature with its first measurement along the vertical direction in laboratory conditions. Previous studies numerically identified the near-zone and polar-region problems for gravitational curvature of a tesseroid, but these issues remain unresolved. In this contribution, we derive the new third-order central and single-sided difference formulas with one, two, and three arguments using the finite difference method. To solve these near-zone and polar-region problems, we apply a numerical approach combining the conditional split, finite difference, and double exponential rule based on these newly derived third-order difference formulas when the computation point is located below, inside, and outside the tesseroid. Numerical experiments with a spherical shell discretized into tesseroids reveal that the accuracy of gravitational curvature is about 4–8 digits in double precision. Numerical results confirm that when the computation point moves to the surface of the tesseroid, the relative and absolute errors of gravitational curvature do not change much, i.e., the near-zone problem can be adequately solved using the numerical approach in this study. When the latitude of the computation point increases, the relative and absolute errors of gravitational curvature do not increase, which solves the polar-region problem with this stable numerical approach. The provided Fortran codes at https://github.com/xiaoledeng/xtessgc-xqtessgc will help with potential applications for the gravitational field of different celestial bodies in geodesy, geophysics, and planetary sciences.

Keywords Gravitational field · Gravity forward modeling · Gravitational curvature · Tesseroid · Numerical integration

1 Introduction

Computing the planet's gravitational field when the computation point is located inside and outside the planet is a fundamental topic in geodesy, geophysics, and planetary sciences. Generally, the primary quantities of the gravitational field involve gravitational potential and its gradients, including first-order gradient (i.e. gravitational (acceleration) vector), second-order gradient (i.e. gravitational gradient tensor), and third-order gradient (i.e., gravitational curvature, where its physical meaning is the spatial change of the gravitational gradient tensor in different directions). In a more general sense, they are all gradient tensors of the respective order, e.g. zero, one, two, and three.

Following the same framework for formulas of gravitational potential, gravitational vector, and gravitational gradient tensor in Eqs. (1–3) of Fukushima (2018), the expression for gravitational curvature as $\mathbf{G}(\mathbf{X})$ can be presented as:

$$\begin{aligned}\mathbf{G}(\mathbf{X}) &= \frac{\partial^3 V(\mathbf{X})}{\partial \mathbf{X}\partial \mathbf{X}\partial \mathbf{X}} \\ &= G\int\int\int \frac{\rho(\mathbf{x})}{|\mathbf{x}-\mathbf{X}|^7}\cdot \\ &\quad \Big[15(\mathbf{x}-\mathbf{X})\otimes(\mathbf{x}-\mathbf{X})\otimes(\mathbf{x}-\mathbf{X}) \\ &\quad -3(\mathbf{x}-\mathbf{X})|\mathbf{x}-\mathbf{X}|^2\epsilon_{ijk}\Big]\mathrm{d}^3\mathbf{x} \end{aligned} \tag{1}$$

$$\epsilon_{ijk} = \begin{cases} 0 & i \neq j \neq k \\ 3 & i = j = k \\ 1 & \text{otherwise} \end{cases} \tag{2}$$

where G is the gravitational constant. $\mathbf{x}$ and $\mathbf{X}$ are the position vectors of the source mass element and computation (or field) point, respectively. $\rho(\mathbf{x})$ is the density of the source mass element. ϵ_{ijk} is obtained from the summation of the Kronecker delta three times with different indices i, j, and k

✉ Xiao-Le Deng
xiaole.deng@gis.uni-stuttgart.de; xldeng@whu.edu.cn

[1] Institute of Geodesy, University of Stuttgart, 70174 Stuttgart, Germany

of the position vector. Note that the integration domain can be chosen as different layers for various celestial bodies (e.g., Earth, the Moon, and Mars).

The first measurement of gravitational curvature along the vertical direction was performed with the atom interferometry sensors in laboratory conditions (Rosi et al. 2015). With the development of measurement technology, it is hoped to measure gravitational curvature using ground, shipborne, airborne, and satellite gravimetry in the future. In previous studies, gravitational curvature can capture finer details in edge detection and shallow structure recognition, allowing for more precise analysis and interpretation of the topographic and sedimental effects (Deng and Shen 2019; Novák et al. 2019). This study focuses on the numerical calculation of gravitational curvature. Currently, there are two primary numerical methods to calculate gravitational curvature: one is in the spectral domain, and the other is in the spatial domain. In the spatial domain, the different primary mass bodies were adopted to represent the source integration mass bodies for the evaluation of gravitational curvature, e.g., the general volumetric mass bodies (Šprlák and Novák 2015), a rectangular prism (Nagy et al. 2000; Qiu et al. 2019), a sphere (Du and Qiu 2019), a spherical shell, a spherical zonal band (Deng and Sneeuw 2023), and a tesseroid (Deng and Shen 2018a, b, 2019; Deng 2023b; Deng and Sneeuw 2023). In the spectral domain, the expressions of gravitational curvature were presented in the forms of spherical harmonics expansion (Šprlák and Novák 2016, 2017; Šprlák et al. 2016; Ghobadi-Far et al. 2016; Hamáčková et al. 2016; Pitoňák et al. 2018; 2020; Romeshkani et al. 2019; 2021; Novák et al. 2017; 2019; 2021; Šprlák and Pitoňák 2024a, b).

Among the numerical approaches for calculating gravitational curvature of a tesseroid in the spatial domain, there was the near-zone problem of gravitational curvature for the Taylor series expansion (Deng and Shen 2018a, b), Gauss–Legendre quadrature (Deng and Shen 2018b; Deng 2023b), and the adaptive discretization stack-based Gauss–Legendre quadrature (Deng and Shen 2019). Specifically, when the computation point gets close to the surface of the tesseroid, significant errors would be obtained for gravitational curvature using these numerical approaches; see Fig. 4 of Deng and Shen (2018a), Figs. 3, 5 of Deng and Shen (2018b), Fig. 5 of Deng and Shen (2019), and Fig. 4 of Deng (2023b). The polar-region problem occurs when the computation point is close to the polar region due to the change of the tesseroid's geometrical shape to the triangular spherical prism (Ouyang et al. 2024). In other words, the calculation errors of the tesseroid will increase when the computation point moves close to the polar region; see Fig. 8 of Deng and Shen (2018a), Fig. 6 of Deng and Shen (2018b), and Fig. 5 of Deng (2023b). In addition, the situation when the computation point is located inside the tesseroid has yet to be investigated for gravitational curvature. Although the near-zone and polar-region problems for gravitational curvature of the tesseroid were numerically identified (Deng and Shen 2018a, b, 2019; Deng 2023b), these issues remain unresolved. Different from previous studies, this paper focuses on solving the near-zone and polar-region problems for gravitational curvature of a tesseroid. Moreover, this study will study the situation of the computation point located inside the tesseroid for gravitational curvature.

In the previous work, Fukushima (2018) presented a numerical approach by combining the conditional split, finite difference, and double exponential rule (Takahasi and Mori 1973, 1974; Fukushima 2017) to accurately calculate gravitational potential, gravitational vector, and gravitational gradient tensor no matter where the computation point is located inside, on the surface of, near the surface of, or outside the tesseroid. Deng (2023a) corrected the Fortran codes offered by Fukushima (2018) to compute two gravitational vector components (g_Φ and g_Λ) and six gravitational gradient tensor components ($\Gamma_{\Phi\Phi}$, $\Gamma_{\Phi\Lambda}$, $\Gamma_{\Phi H}$, $\Gamma_{\Lambda\Lambda}$, $\Gamma_{\Lambda H}$, and Γ_{HH}). When applying the finite difference approach for the evaluation of gravitational curvature of the tesseroid, one of the theoretical challenges is to derive the third-order finite difference formulas with different arguments. Because there are three main types of third-order finite difference formulas. For instance, the general third-order central and single-sided finite difference formulas with one argument; mixed third-order central and single-sided finite difference formulas with two arguments; and mixed third-order central and single-sided finite difference formulas with three arguments. Different types have complicated forms, especially for two and three arguments.

This study goes beyond the previous studies in that we derive the new third-order central and single-sided finite difference formulas with one argument, two arguments, and three arguments. Based on these newly derived formulas, we have applied the finite difference approach to compute gravitational curvature of a tesseroid in relation with gravitational potential, gravitational vector, and gravitational gradient tensor (Fukushima 2018; Deng 2023a). Numerical experiments with the influences of the height and latitude of the computation point are performed with different grid sizes of the discretized tesseroids to reveal whether the near-zone and polar-region problems are solved. The proposed numerical approach for gravitational curvature of a tesseroid can expand the scope of evaluating gravitational curvature of a tesseroid, mainly when the computation point is located near the surface of and inside the tesseroid, which will help to investigate potential applications of gravitational curvature for the topographic effects, crustal effects, and other layers of the celestial bodies (e.g., Earth, the Moon, and Mars) in geodesy, geophysics, and planetary sciences.

This paper is structured as follows: Section 2 presents the theoretical parts of this paper, in which the third-order central

Table 1 Expressions for the first- and second-order central finite difference formulas, single-sided finite difference formulas, and their relative errors from Eqs. (72–79) in Appendices C.1 and C.2 of Fukushima (2018)

Name	Notation	Expression
First-order central finite difference formula	$g_0(t)$	$\frac{f(t+\Delta t)-f(t-\Delta t)}{2\Delta t}$
First-order single-sided finite difference formula	$g_\pm(t)$	$\frac{-f(t\pm 2\Delta t)+4f(t\pm\Delta t)-3f(t)}{\pm 2\Delta t}$
Second-order central finite difference formula	$h_0(t)$	$\frac{f(t+\Delta t)-2f(t)+f(t-\Delta t)}{(\Delta t)^2}$
Second-order single-sided finite difference formula	$h_\pm(t)$	$\frac{-f(t\pm 3\Delta t)+4f(t\pm 2\Delta t)-5f(t\pm\Delta t)+2f(t)}{(\Delta t)^2}$
Relative error of $g_0(t)$	$\delta g_0(t)$	$\frac{g_0(t)-f^{(1)}(t)}{f^{(1)}(t)} \approx \left(\frac{f^{(3)}(t)}{6f^{(1)}(t)}\right)(\Delta t)^2$
Relative error of $g_\pm(t)$	$\delta g_\pm(t)$	$\frac{g_\pm(t)-f^{(1)}(t)}{f^{(1)}(t)} \approx -\left(\frac{f^{(3)}(t)}{3f^{(1)}(t)}\right)(\Delta t)^2$
Relative error of $h_0(t)$	$\delta h_0(t)$	$\frac{h_0(t)-f^{(2)}(t)}{f^{(2)}(t)} \approx \left(\frac{f^{(4)}(t)}{12f^{(2)}(t)}\right)(\Delta t)^2$ *
Relative error of $h_\pm(t)$	$\delta h_\pm(t)$	$\frac{h_\pm(t)-f^{(2)}(t)}{f^{(2)}(t)} \approx -\left(\frac{11f^{(4)}(t)}{12f^{(2)}(t)}\right)(\Delta t)^2$

*From Deng (2023a)

and single-sided finite difference formulas with one argument, two arguments, and three arguments are derived in Sects. 2.1, 2.2, and 2.3, respectively. The numerical computation of gravitational curvature of a tesseroid is presented in Sect. 2.4. Section 3 performs the numerical experiments. The setup of the numerical investigations is described in Sect. 3.1. Section 3.2 calculates the computation time of gravitational potential, gravitational vector, gravitational gradient tensor, and gravitational curvature. The influences of the height and latitude of the computation point on gravitational curvature are studied in Sects. 3.3 and 3.5, respectively. Sections 3.4 and 3.6 investigate the grid size effects with the influences of the height and latitude on gravitational curvature, respectively. Finally, the conclusions and outlook are presented in Sect. 4.

2 Theoretical aspects

2.1 General third-order central and single-sided finite difference formulas with one argument

The first- and second-order central finite difference formulas, single-sided finite difference formulas, and their relative errors were derived in Appendices C.1 and C.2 of Fukushima (2018). To keep the derivation process in this section consistent with that in Eqs. (72–79) in Appendices C.1 and C.2 of Fukushima (2018), the related expressions are presented in Table 1. In this section, we will derive the third-order and single-sided central finite difference formulas with one argument.

If a function $f(t)$ is analytic in a interval $[t-4\Delta t, t+4\Delta t]$, the third-order central finite difference formula $f^{(3)}(t)$ can be obtained by taking first-order derivative on the second-order central finite difference formula $h_0(t)$ in Table 1 with respect to t as:

$$\begin{aligned} f^{(3)}(t) &= \frac{\partial^3 f(t)}{\partial t^3} = \frac{\partial f^{(2)}(t)}{\partial t} \approx k_0(t) = \frac{\partial h_0(t)}{\partial t} \\ &= \frac{f(t+2\Delta t)-2f(t+\Delta t)+2f(t-\Delta t)-f(t-2\Delta t)}{2(\Delta t)^3} \end{aligned} \tag{3}$$

where $f^{(n)}$ represents a general form of the nth-order derivative of the function f.

In Eq. (3), $f(t\pm 2\Delta t)$ and $f(t\pm\Delta t)$ can be expressed by the Taylor series expansion as:

$$\begin{aligned} f(t\pm 2\Delta t) &= f(t) \pm 2\Delta t f^{(1)}(t) + \frac{1}{2}(\pm 2)^2(\Delta t)^2 f^{(2)}(t) \\ &\quad + \frac{1}{6}(\pm 2)^3(\Delta t)^3 f^{(3)}(t) + \frac{1}{24}(\pm 2)^4(\Delta t)^4 f^{(4)}(t) \\ &\quad + \frac{1}{120}(\pm 2)^5(\Delta t)^5 f^{(5)}(t) + \mathcal{O}((\Delta t)^6) \end{aligned} \tag{4}$$

$$\begin{aligned} f(t\pm\Delta t) &= f(t) \pm \Delta t f^{(1)}(t) + \frac{1}{2}(\pm 1)^2(\Delta t)^2 f^{(2)}(t) \\ &\quad + \frac{1}{6}(\pm 1)^3(\Delta t)^3 f^{(3)}(t) + \frac{1}{24}(\pm 1)^4(\Delta t)^4 f^{(4)}(t) \\ &\quad + \frac{1}{120}(\pm 1)^5(\Delta t)^5 f^{(5)}(t) + \mathcal{O}((\Delta t)^6) \end{aligned} \tag{5}$$

where $\mathcal{O}((\Delta t)^6)$ represents higher-order terms of the Taylor series. If omitted in the series, this term represents the approximation error.

Substituting Eqs. (4–5) into Eq. (3), the relative error $\delta k_0(t)$ of the third-order central finite difference formula is obtained as:

$$\delta k_0(t) \equiv \frac{k_0(t) - f^{(3)}(t)}{f^{(3)}(t)} \approx \left(\frac{f^{(5)}(t)}{4f^{(3)}(t)}\right)(\Delta t)^2 \tag{6}$$

If a function $f(t)$ is not analytic in an interval, $f(t)$ will have a discontinuity, a kink, or a singularity within this interval; see Appendix C.1 of Fukushima (2018). When $f(t)$ is not analytic in the interval $[t-4\Delta t, t+4\Delta t]$, the third-order single-sided finite difference formula is denoted as:

$$\begin{aligned} f^{(3)}(t) = \frac{\partial^3 f(t)}{\partial t^3} &\approx k_{\pm}(t) \\ &= af(t \pm 4\Delta t) + bf(t \pm 3\Delta t) + cf(t \pm 2\Delta t) \\ &\quad + df(t \pm \Delta t) + ef(t) \end{aligned} \tag{7}$$

In Eq. (7), $f(t \pm 4\Delta t)$ and $f(t \pm 3\Delta t)$ can be expressed by the Taylor series expansion as:

$$\begin{aligned} f(t \pm 4\Delta t) &= f(t) \pm 4\Delta t f^{(1)}(t) + \frac{1}{2}(\pm 4)^2(\Delta t)^2 f^{(2)}(t) \\ &\quad + \frac{1}{6}(\pm 4)^3(\Delta t)^3 f^{(3)}(t) + \frac{1}{24}(\pm 4)^4(\Delta t)^4 f^{(4)}(t) \\ &\quad + \frac{1}{120}(\pm 4)^5(\Delta t)^5 f^{(5)}(t) + \mathcal{O}((\Delta t)^6) \end{aligned} \tag{8}$$

$$\begin{aligned} f(t \pm 3\Delta t) &= f(t) \pm 3\Delta t f^{(1)}(t) + \frac{1}{2}(\pm 3)^2(\Delta t)^2 f^{(2)}(t) \\ &\quad + \frac{1}{6}(\pm 3)^3(\Delta t)^3 f^{(3)}(t) + \frac{1}{24}(\pm 3)^4(\Delta t)^4 f^{(4)}(t) \\ &\quad + \frac{1}{120}(\pm 3)^5(\Delta t)^5 f^{(5)}(t) + \mathcal{O}((\Delta t)^6) \end{aligned} \tag{9}$$

Substituting Eqs. (4–5) and (8–9) into Eq. (7) yields:

$$\begin{aligned} k_{\pm}(t) &= (a+b+c+d+e)f(t) \\ &\quad \pm (4a+3b+2c+d)\Delta t f^{(1)}(t) \\ &\quad + \frac{1}{2}(16a+9b+4c+d)(\Delta t)^2 f^{(2)}(t) \\ &\quad \pm \frac{1}{6}(64a+27b+8c+d)(\Delta t)^3 f^{(3)}(t) \\ &\quad + \frac{1}{24}(256a+81b+16c+d)(\Delta t)^4 f^{(4)}(t) \\ &\quad \pm \frac{1}{120}(1024a+243b+32c+d)(\Delta t)^5 f^{(5)}(t) \\ &\quad + \mathcal{O}((\Delta t)^6) \end{aligned} \tag{10}$$

where $k_{\pm}(t)$ will be represented by the third- and fifth-order derivatives, while other order (i.e., first-, second-, and fourth-order) derivatives and $f(t)$ will become zero. This helps to obtain the detailed expressions for the a, b, c, d, and e.

Letting

$$\begin{cases} a+b+c+d+e = 0 \\ 4a+3b+2c+d = 0 \\ 16a+9b+4c+d = 0 \\ \pm\frac{1}{6}(64a+27b+8c+d) = \frac{1}{(\Delta t)^3} \\ 256a+81b+16c+d = 0 \end{cases} \tag{11}$$

yields:

$$\begin{cases} a = \dfrac{-3}{\pm 2(\Delta t)^3} \\ b = \dfrac{7}{\pm(\Delta t)^3} \\ c = \dfrac{-12}{\pm(\Delta t)^3} \\ d = \dfrac{9}{\pm(\Delta t)^3} \\ e = \dfrac{-5}{\pm 2(\Delta t)^3} \end{cases} \tag{12}$$

Substituting Eq. (12) into Eq. (7), the third-order single-sided finite difference formula is obtained as:

$$\begin{aligned} k_{\pm}(t) = \frac{1}{\pm 2(\Delta t)^3}\big[&-3f(t \pm 4\Delta t) + 14f(t \pm 3\Delta t) \\ &- 24f(t \pm 2\Delta t) + 18f(t \pm \Delta t) - 5f(t)\big] \end{aligned} \tag{13}$$

where the sign $\pm$ depends on the analyticity of $f(t)$. For example, the positive sign $(+)$ is chosen if $f(t)$ is analytic in the interval $[t, t+4\Delta t]$ and the negative sign $(-)$ is chosen if $f(t)$ is analytic in the interval $[t-4\Delta t, t]$.

Substituting Eq. (12) into Eq. (10), the relative error $\delta k_{\pm}(t)$ of the third-order single-sided finite difference formula can be obtained as:

$$\delta k_{\pm}(t) = \frac{k_{\pm}(t) - f^{(3)}(t)}{f^{(3)}(t)} \approx -\left(\frac{7f^{(5)}(t)}{4f^{(3)}(t)}\right)(\Delta t)^2 \tag{14}$$

where the magnitude of Eq. (14) is 7 times larger than that of Eq. (6).

2.2 Mixed third-order central and single-sided finite difference formulas with two arguments

The function with two arguments is assumed to be $f(u, v)$ for simplicity. In this section, the $\partial^3 f/(\partial u^2\, \partial v)$ is adopted, and the below formulas can be applied by exchanging the roles of u and v for the $\partial^3 f/(\partial u\, \partial^2 v)$.

The mixed third-order partial derivatives are obtained by mixing the second-order central finite difference formula

$h_0(u)$ in Table 1 with respect to u and the first-order central finite difference formula $g_0(v)$ in Table 1 with respect to v as:

$$\begin{aligned}\frac{\partial^3 f}{\partial u^2 \partial v} \approx \frac{1}{2(\Delta u)^2(\Delta v)}\big[& f(u+\Delta u, v+\Delta v) \\ & - f(u+\Delta u, v-\Delta v) - 2f(u, v+\Delta v) \\ & + 2f(u, v-\Delta v) + f(u-\Delta u, v+\Delta v) \\ & - f(u-\Delta u, v-\Delta v)\big] \end{aligned} \tag{15}$$

In addition, if $f(u, v)$ is analytic with respect to u but not with respect to v, the mixed third-order partial derivatives are approximated by mixing the second-order central finite difference formula $h_0(u)$ in Table 1 with respect to u and the first-order single-sided finite difference formula $g_\pm(v)$ in Table 1 with respect to v as follows:

$$\begin{aligned}\frac{\partial^3 f}{\partial u^2 \partial v} \approx \frac{\epsilon_v}{2(\Delta u)^2(\Delta v)}\big[& - f(u+\Delta u, v+2\epsilon_v\Delta v) \\ & + 4f(u+\Delta u, v+\epsilon_v\Delta v) - 3f(u+\Delta u, v) \\ & + 2f(u, v+2\epsilon_v\Delta v) - 8f(u, v+\epsilon_v\Delta v) \\ & + 6f(u, v) - f(u-\Delta u, v+2\epsilon_v\Delta v) \\ & + 4f(u-\Delta u, v+\epsilon_v\Delta v) - 3f(u-\Delta u, v)\big] \end{aligned} \tag{16}$$

where $\epsilon_v = \pm 1$ is the sign factor depending on the specific situation, e.g. $\epsilon_v = 1$ when $f(t)$ is analytic in the interval $[t, t+\Delta t]$ and $\epsilon_v = -1$ when $f(t)$ is analytic in the interval $[t-\Delta t, t]$.

When $f(u, v)$ is analytic with respect to v but not with respect to u, the mixed third-order partial derivatives are computed by mixing the second-order single-sided finite difference formula $h_\pm(u)$ in Table 1 with respect to u and the first-order central finite difference formula $g_0(v)$ in Table 1 with respect to v as:

$$\begin{aligned}\frac{\partial^3 f}{\partial u^2 \partial v} \approx \frac{1}{2(\Delta u)^2(\Delta v)}\big[& - f(u+3\epsilon_u\Delta u, v+\Delta v) \\ & + f(u+3\epsilon_u\Delta u, v-\Delta v) \\ & + 4f(u+2\epsilon_u\Delta u, v+\Delta v) \\ & - 4f(u+2\epsilon_u\Delta u, v-\Delta v) \\ & - 5f(u+\epsilon_u\Delta u, v+\Delta v) \\ & + 5f(u+\epsilon_u\Delta u, v-\Delta v) \\ & + 2f(u, v+\Delta v) - 2f(u, v-\Delta v)\big] \end{aligned} \tag{17}$$

where $\epsilon_u = \pm 1$ is the sign factor depending on the specific situation, e.g., $\epsilon_u = 1$ when $f(t)$ is analytic in the interval $[t, t+\Delta t]$ and $\epsilon_u = -1$ when $f(t)$ is analytic in the interval $[t-\Delta t, t]$.

Finally, if $f(u, v)$ is not analytic with respect to both u and v, the mixed third-order partial derivatives are obtained by mixing the second-order single-sided finite difference formula $h_\pm(u)$ in Table 1 with respect to u and the first-order single-sided finite difference formula $g_\pm(v)$ in Table 1 with respect to v as:

$$\begin{aligned}\frac{\partial^3 f}{\partial u^2 \partial v} \approx \frac{\epsilon_v}{2(\Delta u)^2(\Delta v)}\big[& f(u+3\epsilon_u\Delta u, v+2\epsilon_v\Delta v) \\ & - 4f(u+3\epsilon_u\Delta u, v+\epsilon_v\Delta v) \\ & + 3f(u+3\epsilon_u\Delta u, v) \\ & - 4f(u+2\epsilon_u\Delta u, v+2\epsilon_v\Delta v) \\ & + 16f(u+2\epsilon_u\Delta u, v+\epsilon_v\Delta v) \\ & - 12f(u+2\epsilon_u\Delta u, v) \\ & + 5f(u+\epsilon_u\Delta u, v+2\epsilon_v\Delta v) \\ & - 20f(u+\epsilon_u\Delta u, v+\epsilon_v\Delta v) \\ & + 15f(u+\epsilon_u\Delta u, v) - 2f(u, v+2\epsilon_v\Delta v) \\ & + 8f(u, v+\epsilon_v\Delta v) - 6f(u, v)\big] \end{aligned} \tag{18}$$

where $\epsilon_u = \pm 1$ and $\epsilon_v = \pm 1$ are the sign factors depending on the specific situations described above.

2.3 Mixed third-order central and single-sided finite difference formulas with three arguments

This section sets the function with three arguments as $f(u, v, w)$. Regarding the mixed third-order partial derivatives with three arguments (i.e., $\partial^3 f/(\partial u \partial v \partial w)$), each variable (i.e., u, v, and w) has two forms, i.e., the first-order central finite difference formula (i.e., u_0, v_0, and w_0) and the first-order single-sided finite difference formula (i.e., $u_\pm$, $v_\pm$, and $w_\pm$). Thus, there are $2 \times 2 \times 2 = 8$ combinations in total (i.e., $\{u_0, v_0, w_0\}$, $\{u_0, v_0, w_\pm\}$, $\{u_0, v_\pm, w_0\}$, $\{u_0, v_\pm, w_\pm\}$, $\{u_\pm, v_0, w_0\}$, $\{u_\pm, v_0, w_\pm\}$, $\{u_\pm, v_\pm, w_0\}$, and $\{u_\pm, v_\pm, w_\pm\}$). Among these eight combinations, there are four classifications:

(1) three variables with first-order central finite difference formulas, i.e., $\{u_0, v_0, w_0\}$;
(2) two variables with first-order central finite difference formulas and one variable with first-order single-sided finite difference formula, i.e., $\{u_0, v_0, w_\pm\}$, $\{u_0, v_\pm, w_0\}$, and $\{u_\pm, v_0, w_0\}$;
(3) one variable with first-order central finite difference formula and two variables with first-order single-sided finite difference formulas, i.e., $\{u_0, v_\pm, w_\pm\}$, $\{u_\pm, v_0, w_\pm\}$, and $\{u_\pm, v_\pm, w_0\}$;
(4) three variables with first-order single-sided finite difference formulas, i.e., $\{u_\pm, v_\pm, w_\pm\}$.

Herein, only one situation in the four classifications is described for simplicity.

If $f(u, v, w)$ is analytic with respect to u, v, and w (i.e. $\{u_0, v_0, w_0\}$), the mixed third-order partial derivatives are obtained by repeatedly using the first-order central finite difference formulas (i.e., $g_0(u)$, $g_0(v)$, and $g_0(w)$) in Table 1 three times as:

$$\begin{aligned}\frac{\partial^3 f}{\partial u\partial v\partial w} \approx \frac{1}{8(\Delta u)(\Delta v)(\Delta w)}\big[& \\ & f(u+\Delta u, v+\Delta v, w+\Delta w)\\ & - f(u+\Delta u, v+\Delta v, w-\Delta w)\\ & - f(u+\Delta u, v-\Delta v, w+\Delta w)\\ & + f(u+\Delta u, v-\Delta v, w-\Delta w)\\ & - f(u-\Delta u, v+\Delta v, w+\Delta w)\\ & + f(u-\Delta u, v+\Delta v, w-\Delta w)\\ & + f(u-\Delta u, v-\Delta v, w+\Delta w)\\ & - f(u-\Delta u, v-\Delta v, w-\Delta w)\big]\end{aligned} \tag{19}$$

If $f(u, v, w)$ is analytic with respect to u and v but not with respect to w (i.e., $\{u_0, v_0, w_\pm\}$), the mixed third-order partial derivatives are presented by mixing the first-order central finite difference formulas in Table 1 with respect to u and v (i.e., $g_0(u)$ and $g_0(v)$) twice and the first-order single-sided finite difference formula in Table 1 with respect to w (i.e., $g_\pm(w)$) as:

$$\begin{aligned}\frac{\partial^3 f}{\partial u\partial v\partial w} \approx \frac{\epsilon_w}{8(\Delta u)(\Delta v)(\Delta w)}\big[& \\ & - f(u+\Delta u, v+\Delta v, w+2\epsilon_w\Delta w)\\ & + 4f(u+\Delta u, v+\Delta v, w+\epsilon_w\Delta w)\\ & - 3f(u+\Delta u, v+\Delta v, w)\\ & + f(u+\Delta u, v-\Delta v, w+2\epsilon_w\Delta w)\\ & - 4f(u+\Delta u, v-\Delta v, w+\epsilon_w\Delta w)\\ & + 3f(u+\Delta u, v-\Delta v, w)\\ & + f(u-\Delta u, v+\Delta v, w+2\epsilon_w\Delta w)\\ & - 4f(u-\Delta u, v+\Delta v, w+\epsilon_w\Delta w)\\ & + 3f(u-\Delta u, v+\Delta v, w)\\ & - f(u-\Delta u, v-\Delta v, w+2\epsilon_w\Delta w)\\ & + 4f(u-\Delta u, v-\Delta v, w+\epsilon_w\Delta w)\\ & - 3f(u-\Delta u, v-\Delta v, w)\big]\end{aligned} \tag{20}$$

When $f(u, v, w)$ is analytic with respect to u but not with respect to v and w (i.e., $\{u_0, v_\pm, w_\pm\}$), the mixed third-order partial derivatives are computed by mixing the first-order central finite difference formula in Table 1 with respect to u (i.e., $g_0(u)$) and the first-order single-sided finite difference formulas in Table 1 with respect to v and w twice (i.e., $g_\pm(v)$ and $g_\pm(w)$) as:

$$\begin{aligned}\frac{\partial^3 f}{\partial u\partial v\partial w} \approx \frac{\epsilon_v\epsilon_w}{8(\Delta u)(\Delta v)(\Delta w)}\big[& \\ & f(u+\Delta u, v+2\epsilon_v\Delta v, w+2\epsilon_w\Delta w)\\ & - 4f(u+\Delta u, v+2\epsilon_v\Delta v, w+\epsilon_w\Delta w)\\ & + 3f(u+\Delta u, v+2\epsilon_v\Delta v, w)\\ & - 4f(u+\Delta u, v+\epsilon_v\Delta v, w+2\epsilon_w\Delta w)\\ & + 16f(u+\Delta u, v+\epsilon_v\Delta v, w+\epsilon_w\Delta w)\\ & - 12f(u+\Delta u, v+\epsilon_v\Delta v, w)\\ & + 3f(u+\Delta u, v, w+2\epsilon_w\Delta w)\\ & - 12f(u+\Delta u, v, w+\epsilon_w\Delta w)\\ & + 9f(u+\Delta u, v, w)\\ & - f(u-\Delta u, v+2\epsilon_v\Delta v, w+2\epsilon_w\Delta w)\\ & + 4f(u-\Delta u, v+2\epsilon_v\Delta v, w+\epsilon_w\Delta w)\\ & - 3f(u-\Delta u, v+2\epsilon_v\Delta v, w)\\ & + 4f(u-\Delta u, v+\epsilon_v\Delta v, w+2\epsilon_w\Delta w)\\ & - 16f(u-\Delta u, v+\epsilon_v\Delta v, w+\epsilon_w\Delta w)\\ & + 12f(u-\Delta u, v+\epsilon_v\Delta v, w)\\ & - 3f(u-\Delta u, v, w+2\epsilon_w\Delta w)\\ & + 12f(u-\Delta u, v, w+\epsilon_w\Delta w)\\ & - 9f(u-\Delta u, v, w)\big]\end{aligned} \tag{21}$$

Finally, if $f(u, v, w)$ is not analytic with respect to u, v, and w (i.e., $\{u_\pm, v_\pm, w_\pm\}$), the mixed third-order partial derivatives are obtained by repeatedly using the first-order single-sided finite difference formulas in Table 1 (i.e. $g_\pm(u)$, $g_\pm(v)$, and $g_\pm(w)$) three times as:

$$\begin{aligned}\frac{\partial^3 f}{\partial u\partial v\partial w} \approx \frac{\epsilon_u\epsilon_v\epsilon_w}{8(\Delta u)(\Delta v)(\Delta w)}\big[& \\ & - f(u+2\epsilon_u\Delta u, v+2\epsilon_v\Delta v, w+2\epsilon_w\Delta w)\\ & + 4f(u+2\epsilon_u\Delta u, v+2\epsilon_v\Delta v, w+\epsilon_w\Delta w)\\ & - 3f(u+2\epsilon_u\Delta u, v+2\epsilon_v\Delta v, w)\\ & + 4f(u+2\epsilon_u\Delta u, v+\epsilon_v\Delta v, w+2\epsilon_w\Delta w)\\ & - 16f(u+2\epsilon_u\Delta u, v+\epsilon_v\Delta v, w+\epsilon_w\Delta w)\\ & + 12f(u+2\epsilon_u\Delta u, v+\epsilon_v\Delta v, w)\\ & - 3f(u+2\epsilon_u\Delta u, v, w+2\epsilon_w\Delta w)\\ & + 12f(u+2\epsilon_u\Delta u, v, w+\epsilon_w\Delta w)\\ & - 9f(u+2\epsilon_u\Delta u, v, w)\\ & + 4f(u+\epsilon_u\Delta u, v+2\epsilon_v\Delta v, w+2\epsilon_w\Delta w)\\ & - 16f(u+\epsilon_u\Delta u, v+2\epsilon_v\Delta v, w+\epsilon_w\Delta w)\\ & + 12f(u+\epsilon_u\Delta u, v+2\epsilon_v\Delta v, w)\\ & - 16f(u+\epsilon_u\Delta u, v+\epsilon_v\Delta v, w+2\epsilon_w\Delta w)\\ & + 64f(u+\epsilon_u\Delta u, v+\epsilon_v\Delta v, w+\epsilon_w\Delta w)\end{aligned}$$

$$
\begin{aligned}
&- 48 f(u + \epsilon_u \Delta u, v + \epsilon_v \Delta v, w) \\
&+ 12 f(u + \epsilon_u \Delta u, v, w + 2\epsilon_w \Delta w) \\
&- 48 f(u + \epsilon_u \Delta u, v, w + \epsilon_w \Delta w) \\
&+ 36 f(u + \epsilon_u \Delta u, v, w) \\
&- 3 f(u, v + 2\epsilon_v \Delta v, w + 2\epsilon_w \Delta w) \\
&+ 12 f(u, v + 2\epsilon_v \Delta v, w + \epsilon_w \Delta w) \\
&- 9 f(u, v + 2\epsilon_v \Delta v, w) \\
&+ 12 f(u, v + \epsilon_v \Delta v, w + 2\epsilon_w \Delta w) \\
&- 48 f(u, v + \epsilon_v \Delta v, w + \epsilon_w \Delta w) \\
&+ 36 f(u, v + \epsilon_v \Delta v, w) \\
&- 9 f(u, v, w + 2\epsilon_w \Delta w) \\
&+ 36 f(u, v, w + \epsilon_w \Delta w) - 27 f(u, v, w)\big]
\end{aligned} \tag{22}
$$

The above sign factors $\epsilon_u = \pm 1$, $\epsilon_v = \pm 1$, and $\epsilon_w = \pm 1$ in Eqs. (20–22) should be chosen based on the specific situations.

It should be noted that the expressions for the mixed third-order partial derivatives of other different situations $\{u_0, v_\pm, w_0\}$ (or $\{u_\pm, v_0, w_0\}$) and $\{u_\pm, v_0, w_\pm\}$ (or $\{u_\pm, v_\pm, w_0\}$) can be obtained based on those of the $\{u_\pm, v_0, w_0\}$ and $\{u_0, v_\pm, w_\pm\}$ in Eqs. (20) and (21), respectively.

2.4 Computation of gravitational curvature of a tesseroid

Based on these newly derived third-order central and single-sided finite difference formulas with one, two, and three arguments in Sects. 2.1–2.3, this section presents the details to calculate gravitational curvature of a tesseroid. Regarding gravitational curvature of a tesseroid, their expressions were derived from spherical integral kernels in Deng and Shen (2018a) and Cartesian integral kernels in Deng and Shen (2018b), respectively. Different from Deng and Shen (2018a, b), this study obtains third-order partial derivatives of gravitational potential from the third-order central and single-sided finite difference formulas with one, two, and three arguments in the form of the Taylor series expansion. Specifically, different conditional switches of the above-mentioned third-order difference formulas in Sects. 2.1–2.3 are used for the numerical differentiation of gravitational curvature.

The third-order partial derivatives of gravitational potential (V) are derived with the polynomials of the Taylor series expansion. The functions in the Taylor series expansion contain the combination of gravitational potential, where its numerical integration for a tesseroid is provided in Sect. 2.1 of Fukushima (2018). The ten defining components of the third-order partial derivatives can be divided into three categories:

(1) the diagonal components, i.e., $(\partial^3 V/\partial \Phi^3)_{\Lambda,H}$, $(\partial^3 V/\partial \Lambda^3)_{\Phi,H}$, and $(\partial^3 V/\partial H^3)_{\Phi,\Lambda}$;
(2) the non-diagonal components with two different variables among three spatial variables Φ, Λ, and H, i.e., $[\partial^3 V/(\partial \Phi^2 \partial \Lambda)]_H$, $[\partial^3 V/(\partial \Phi^2 \partial H)]_\Lambda$, $[\partial^3 V/(\partial \Phi \partial \Lambda^2)]_H$, $[\partial^3 V/(\partial \Lambda^2 \partial H)]_\Phi$, $[\partial^3 V/(\partial \Phi \partial H^2)]_\Lambda$, and $[\partial^3 V/(\partial \Lambda \partial H^2)]_\Phi$;
(3) the non-diagonal components with three different spatial variables Φ, Λ, and H, i.e., $\partial^3 V/(\partial \Phi \partial \Lambda \partial H)$.

Three sample expressions for the components of gravitational curvature in these three categories are presented in the form of the Taylor series expansion as follows:

$$
\begin{aligned}
\left(\frac{\partial^3 V}{\partial H^3}\right)_{\Phi,\Lambda} = &\frac{1}{2(\Delta_3 H)^3}\big[V(\Phi, \Lambda, H + 2\Delta_3 H) \\
&- 2V(\Phi, \Lambda, H + \Delta_3 H) \\
&+ 2V(\Phi, \Lambda, H - \Delta_3 H) \\
&- V(\Phi, \Lambda, H - 2\Delta_3 H)\big] \\
&- \frac{(\Delta_3 H)^2}{4}\left(\frac{\partial^5 V}{\partial H^5}\right) - \cdots
\end{aligned} \tag{23}
$$

$$
\begin{aligned}
\left(\frac{\partial^3 V}{\partial \Phi \partial H^2}\right)_{\Lambda} = &\frac{1}{2(\Delta_3 \Phi)(\Delta_3 H)^2}\big[\\
&V(\Phi + \Delta_3 \Phi, \Lambda, H + \Delta_3 H) \\
&- V(\Phi - \Delta_3 \Phi, \Lambda, H + \Delta_3 H) \\
&- 2V(\Phi + \Delta_3 \Phi, \Lambda, H) \\
&+ 2V(\Phi - \Delta_3 \Phi, \Lambda, H) \\
&+ V(\Phi + \Delta_3 \Phi, \Lambda, H - \Delta_3 H) \\
&- V(\Phi - \Delta_3 \Phi, \Lambda, H - \Delta_3 H)\big] \\
&- \frac{(\Delta_3 \Phi)^2}{6}\left(\frac{\partial^5 V}{\partial \Phi^3 \partial H^2}\right) \\
&- \frac{(\Delta_3 H)^2}{12}\left(\frac{\partial^5 V}{\partial \Phi \partial H^4}\right) - \cdots
\end{aligned} \tag{24}
$$

$$
\begin{aligned}
\left(\frac{\partial^3 V}{\partial \Phi \partial \Lambda \partial H}\right) = &\frac{1}{8(\Delta_3 \Phi)(\Delta_3 \Lambda)(\Delta_3 H)} \\
&\big[V(\Phi + \Delta_3 \Phi, \Lambda + \Delta_3 \Lambda, H + \Delta_3 H) \\
&- V(\Phi + \Delta_3 \Phi, \Lambda + \Delta_3 \Lambda, H - \Delta_3 H) \\
&- V(\Phi + \Delta_3 \Phi, \Lambda - \Delta_3 \Lambda, H + \Delta_3 H) \\
&+ V(\Phi + \Delta_3 \Phi, \Lambda - \Delta_3 \Lambda, H - \Delta_3 H) \\
&- V(\Phi - \Delta_3 \Phi, \Lambda + \Delta_3 \Lambda, H + \Delta_3 H) \\
&+ V(\Phi - \Delta_3 \Phi, \Lambda + \Delta_3 \Lambda, H - \Delta_3 H) \\
&+ V(\Phi - \Delta_3 \Phi, \Lambda - \Delta_3 \Lambda, H + \Delta_3 H) \\
&- V(\Phi - \Delta_3 \Phi, \Lambda - \Delta_3 \Lambda, H - \Delta_3 H)\big] \\
&- \frac{(\Delta_3 \Phi)^2}{6}\left(\frac{\partial^5 V}{\partial \Phi^3 \partial \Lambda \partial H}\right)
\end{aligned}
$$

$$-\frac{(\Delta_3\Lambda)^2}{6}\left(\frac{\partial^5 V}{\partial\Phi\partial\Lambda^3\partial H}\right)$$
$$-\frac{(\Delta_3 H)^2}{6}\left(\frac{\partial^5 V}{\partial\Phi\partial\Lambda\partial H^3}\right)-\cdots \quad (25)$$

where (Φ, Λ, H) are the geocentric latitude, longitude, and height measured from the reference spherical surface along the surface normal of the computation point in the spherical Gauss normal coordinates (Fukushima 2018). Note that the higher-order terms (i.e., larger than or equal to fifth-order terms) are truncated for evaluating the third-order partial derivatives in the numerical calculation. If one wants to improve the accuracy of the third-order partial derivatives, fifth-order and higher-order terms in Taylor series expansion should be considered. Based on these new third-order finite difference formulas in Sects. 2.1–2.3, the detailed expressions for the third-order partial derivatives under different situations with the latitude, longitude, and height in different intervals are listed in Appendix A.

Previous test argument displacements were $\Delta_1\Phi$, $\Delta_1\Lambda$, $\Delta_1 H$ for gravitational vector and $\Delta_2\Phi$, $\Delta_2\Lambda$, $\Delta_2 H$ for gravitational gradient tensor in Eqs. (17) and (27) of Fukushima (2018). This study defines the new test argument displacements $\Delta_3\Phi$, $\Delta_3\Lambda$, and $\Delta_3 H$ for gravitational curvature with respect to the spherical latitude Φ, longitude Λ, and height H as:

$$\Delta_3\Phi=\frac{\Delta_3 H}{R},\quad \Delta_3\Lambda=\frac{\Delta_3 H}{R\cos\Phi},\quad \Delta_3 H=L\,\delta_3 \quad (26)$$
$$R=R_0+H \quad (27)$$
$$L=\max(\ell_0,\ell) \quad (28)$$
$$\ell_0=\frac{1}{2}\sqrt{(\Delta H)^2+R_C^2\left[(\Delta\Phi)^2+(\cos\Phi_C)^2(\Delta\Lambda)^2\right]} \quad (29)$$
$$\ell=\sqrt{R^2+R_C^2-2\,R\,R_C\left[\sin\Phi\sin\Phi_C+\cos\Phi\cos\Phi_C\cos(\Lambda-\Lambda_C)\right]} \quad (30)$$
$$\Delta\Phi=\Phi_N-\Phi_S,\quad \Delta\Lambda=\Lambda_E-\Lambda_W,\quad \Delta H=H_T-H_B \quad (31)$$
$$R_C=R_0+\frac{H_T+H_B}{2},\quad \Phi_C=\frac{\Phi_N+\Phi_S}{2},\ \Lambda_C=\frac{\Lambda_E+\Lambda_W}{2} \quad (32)$$

where the parameters R, L, and ℓ_0 are the same as those in Eqs. (18–23) of Fukushima (2018). R is the geocentric distance of the computation point with respect to the center of the reference sphere, whose radius is R_0. L is a scale factor of the maximum between ℓ_0 (i.e., one-half of the nominal linear size of the tesseroid) and ℓ (i.e., the distance between the computation point and the geometrical center of the tesseroid). $\Delta\Phi$, $\Delta\Lambda$, and ΔH are the grid sizes of the tesseroid with respect to the spherical latitudinal, longitudinal, and height directions. The pairs of Φ_N and Φ_S, Λ_E and Λ_W, H_T and H_B are the different latitudinal intervals, longitudinal intervals, and height intervals of the tesseroid with respect to the pairs of North and South, East and West, Top and Bottom endpoints, respectively. R_C, Φ_C, and Λ_C are the geocentric distance, spherical latitude, and longitude of the geometrical center of the tesseroid, respectively.

Previous relative test displacements for gravitational vector and gravitational gradient tensor were $\delta_1=\sqrt[3]{\delta}$ and $\delta_2=\sqrt[4]{\delta}$ in Eq. (34) of Fukushima (2018). This study presents the new relative test displacement δ_3 in Eq. (26) for gravitational curvature as:

$$\delta_3=\sqrt[5]{\delta} \quad (33)$$

where δ is the relative error tolerance in integrating gravitational potential (Fukushima 2018). If $\delta=10^{-33}$ is selected for the quadruple precision environment of gravitational potential (i.e., 33 digits for gravitational potential, 22 digits for gravitational vector, and 16.5 digits for gravitational gradient tensor (Fukushima 2018)), the accuracy of gravitational curvature is expected to be 13.2 digits, which is calculated by:

$$\left|\log_{10}(\delta_3^2)\right|=\left|\log_{10}(\sqrt[5]{\delta^2})\right|=13.2 \quad (34)$$

If $\delta=10^{-16}$ is selected for the double precision environment of gravitational potential (i.e., 16 digits for gravitational potential, 10.67 digits for gravitational vector, and 8 digits for gravitational gradient tensor (Fukushima 2018)), the accuracy of gravitational curvature is expected to be 6.4 digits based on Eq. (34).

The expressions for gravitational curvature ($G_{\alpha\beta\gamma}$ with $\alpha, \beta, \gamma = \Phi, \Lambda, H$) composed of the first-, second-, and third-order partial derivatives can be referred to in Table 4 of Casotto and Fantino (2009). The first- and second-order partial derivatives can be constructed from gravitational vector (g_Φ, g_Λ, and g_H, see Eq. (24) of Fukushima (2018)) and gravitational gradient tensor ($\Gamma_{\Phi\Phi}$, $\Gamma_{\Phi\Lambda}$, $\Gamma_{\Phi H}$, $\Gamma_{\Lambda\Lambda}$, $\Gamma_{\Lambda H}$, and Γ_{HH}, see Eqs. (28–33) of Fukushima (2018); Eqs. (3–4) of Deng (2023a)), where the expressions for these first- and second-order partial derivatives can be referred to in Tables 2–3 of Casotto and Fantino (2009).

Based on Eqs. (24), (28–33) of Fukushima (2018), Eqs. (3–4) of Deng (2023a), and Tables 2–4 of Casotto and Fantino (2009), the final formulas of gravitational curvature are expressed in the forms of the third-order partial derivatives, gravitational vector, and gravitational gradient tensor as:

$$G_{\Phi\Phi\Phi}=\frac{1}{R^3}\left[\left(\frac{\partial^3 V}{\partial\Phi^3}\right)_{\Lambda,H}+R\,(g_\Phi+3R\,\Gamma_{\Phi H})\right] \quad (35)$$
$$G_{\Phi\Phi\Lambda}=\frac{1}{R^3\cos\Phi}\left[\left(\frac{\partial^3 V}{\partial\Phi^2\partial\Lambda}\right)_{H}\right]+\frac{1}{R^2}\left[g_\Lambda+R\,\Gamma_{\Lambda H}+2R\,\tan\Phi\,\Gamma_{\Phi\Lambda}\right] \quad (36)$$
$$G_{\Phi\Phi H}=\frac{1}{R^2}\left[\left(\frac{\partial^3 V}{\partial\Phi^2\partial H}\right)_{\Lambda}+g_H+R\,\Gamma_{HH}-2R\,\Gamma_{\Phi\Phi}\right] \quad (37)$$

$$\mathrm{G}_{\Phi\Lambda H} = \frac{1}{R^2}\Bigg[\frac{1}{\cos\Phi}\left(\frac{\partial^3 V}{\partial\Phi\partial\Lambda\partial H}\right) - 2R\,\Gamma_{\Phi\Lambda} + \tan\Phi\,(g_\Lambda + R\,\Gamma_{\Lambda H})\Bigg] \tag{38}$$

$$\mathrm{G}_{\Lambda\Lambda\Phi} = \frac{\left(\frac{\partial^3 V}{\partial\Phi\partial\Lambda^2}\right)_H - R\,g_\Phi}{R^3\cos^2\Phi} + \frac{1}{R^2}\Big[g_\Phi + R\,\Gamma_{\Phi H} - \tan\Phi\,(g_H - 2R\,\Gamma_{\Lambda\Lambda} + R\,\Gamma_{\Phi\Phi}) + 2\tan^2\Phi\,g_\Phi\Big] \tag{39}$$

$$\mathrm{G}_{\Lambda\Lambda\Lambda} = \frac{R\cos\Phi\,g_\Lambda + \left(\frac{\partial^3 V}{\partial\Lambda^3}\right)_{\Phi,H}}{R^3\cos^3\Phi} + \frac{3\,(\Gamma_{\Lambda H} - \tan\Phi\,\Gamma_{\Phi\Lambda})}{R} \tag{40}$$

$$\mathrm{G}_{\Lambda\Lambda H} = \frac{1}{R^2}\Bigg[g_H + R\Gamma_{HH} - 2R\,\Gamma_{\Lambda\Lambda} + \frac{1}{\cos^2\Phi}\left(\frac{\partial^3 V}{\partial\Lambda^2\partial H}\right)_\Phi - \tan\Phi(g_\Phi + R\,\Gamma_{\Phi H})\Bigg] \tag{41}$$

$$\mathrm{G}_{HH\Phi} = \frac{1}{R}\left[\left(\frac{\partial^3 V}{\partial\Phi\partial H^2}\right)_\Lambda - 2\,\Gamma_{\Phi H}\right] \tag{42}$$

$$\mathrm{G}_{HH\Lambda} = \frac{1}{R}\left[\frac{1}{\cos\Phi}\left(\frac{\partial^3 V}{\partial\Lambda\partial H^2}\right)_\Phi - 2\,\Gamma_{\Lambda H}\right] \tag{43}$$

$$\mathrm{G}_{HHH} = \left(\frac{\partial^3 V}{\partial H^3}\right)_{\Phi,\Lambda} \tag{44}$$

where the validation of the correctness of Eqs. (35–37) and (39–44) is provided in Appendix B.

In Eqs. (35–44), the third-order partial derivatives can be calculated based on detailed expressions for the third-order partial derivatives using different conditional switches in Appendix A. The values of gravitational potential (V), gravitational vector (g_Φ, g_Λ, and g_H), and gravitational gradient tensor ($\Gamma_{\Phi\Phi}$, $\Gamma_{\Phi\Lambda}$, $\Gamma_{\Phi H}$, $\Gamma_{\Lambda\Lambda}$, $\Gamma_{\Lambda H}$, and Γ_{HH}) are obtained using the revised Fortran codes (`xtess.f90` and `xqtess.f90` at https://github.com/xiaoledeng/xtess-xqtess) in double and quadruple precision (Deng 2023a), where the original Fortran codes were from Fukushima (2018).

In this study, Appendix C provides the Fortran codes `xtessgc.f90` and `xqtessgc.f90` at https://github.com/xiaoledeng/xtessgc-xqtessgc to calculate gravitational curvature of a tesseroid, where the main Fortran subroutines and functions are also shown.

3 Numerical investigations

3.1 Setup of the numerical experiments

The numerical setup of the experiments is described as follows. The basic numerical strategy applies the analytical values of gravitational curvature of a spherical shell as references to the calculated values of the discretized tesseroids. The analytical expressions of nonzero gravitational curvature components of a homogenous spherical shell when the computation point is located below ($H < H_B$), inside ($H_B < H < H_T$), and above ($H_T < H$) the spherical shell are presented as:

$$\mathrm{G}_{\Phi\Phi H,\mathrm{analytical}} = \mathrm{G}_{\Lambda\Lambda H,\mathrm{analytical}} = \begin{cases} 0, & (H < H_B) \\ -4\pi G\rho R_B^3/R^4, & (H_B < H < H_T) \\ 3GM/R^4, & (H_T < H) \end{cases} \tag{45}$$

$$\mathrm{G}_{HHH,\mathrm{analytical}} = \begin{cases} 0, & (H < H_B) \\ 8\pi G\rho R_B^3/R^4, & (H_B < H < H_T) \\ -6GM/R^4, & (H_T < H) \end{cases} \tag{46}$$

where M is the mass of the homogenous spherical shell. $M = \frac{4\pi\rho}{3}\left(R_T^2 + R_T R_B + R_B^2\right)\Delta H$ with $R_T = R_0 + H_T$, $R_B = R_0 + H_B$, $R = R_0 + H$, and $\Delta H = H_T - H_B$, which are from Eqs. (49–50) of Fukushima (2018). When the computation points are on the inner and outer boundary of the spherical shell, they are slightly shifted inside the spherical shell; see also Sect. 3.1 of Fukushima (2018) and Sect. 4 of Deng (2023a). Three nonzero components of gravitational curvature satisfy Laplace's equation:

$$\mathrm{G}_{\Phi\Phi H,\mathrm{analytical}} + \mathrm{G}_{\Lambda\Lambda H,\mathrm{analytical}} + \mathrm{G}_{HHH,\mathrm{analytical}} = 0 \tag{47}$$

no matter whether the computation point is located below, inside, or above the spherical shell.

In the following sections, the relative errors in $\log_{10}$ scale are computed for three nonzero gravitational curvature components (i.e., $\delta\mathrm{G}_{\Phi\Phi H}$, $\delta\mathrm{G}_{\Lambda\Lambda H}$, and $\delta\mathrm{G}_{HHH}$; see Eq. (11) of Deng (2023a)) and the absolute errors in $\log_{10}$ scale are calculated for other seven gravitational curvature components (i.e., $\delta\mathrm{G}_{\Phi\Phi\Phi}$, $\delta\mathrm{G}_{\Phi\Phi\Lambda}$, $\delta\mathrm{G}_{\Phi\Lambda H}$, $\delta\mathrm{G}_{\Lambda\Lambda\Phi}$, $\delta\mathrm{G}_{\Lambda\Lambda\Lambda}$, $\delta\mathrm{G}_{HH\Phi}$, and $\delta\mathrm{G}_{HH\Lambda}$). When the computation point is located below the spherical shell (i.e., $H < H_B$), the absolute errors are also computed for these gravitational curvature components $\mathrm{G}_{\Phi\Phi H}$, $\mathrm{G}_{\Lambda\Lambda H}$, and G_{HHH}.

To reveal the internal relation among gravitational curvature components, Laplace's equation parameters in $\log_{10}$ scale of gravitational curvature components are applied as:

$$\delta L_1 = \log_{10}\left(\left|\mathrm{G}_{\Phi\Phi\Phi} + \mathrm{G}_{\Lambda\Lambda\Phi} + \mathrm{G}_{HH\Phi}\right|\right) \tag{48}$$

$$\delta L_2 = \log_{10}\left(\left|\mathrm{G}_{\Phi\Phi\Lambda} + \mathrm{G}_{\Lambda\Lambda\Lambda} + \mathrm{G}_{HH\Lambda}\right|\right) \tag{49}$$

$$\delta L_3 = \log_{10}\left(\left|\mathrm{G}_{\Phi\Phi H} + \mathrm{G}_{\Lambda\Lambda H} + \mathrm{G}_{HHH}\right|\right) \tag{50}$$

where the values of the δL_1, δL_2, and δL_3 are theoretically equal to zero, and their numerical values reflect the levels of the internal numerical precision.

The numerical values in the following experiments are listed in Table 2. The bottom and top heights of the

Table 2 Numerical values in the following experiments

Parameter	Notation	Magnitude	Unit
Newtonian gravitational constant multiplied by the density	$G\rho$	1	s^{-2}
Radius of the reference sphere	R_0	6380	km
Bottom height of the spherical shell	H_B	−40	km
Top height of the spherical shell	H_T	10	km

tesseroids are the same as those of the spherical shell. The selected numerical values are the same as those in Sect. 3.1 of Fukushima (2018) and Sect. 4 of Deng (2023a). When calculating the numerical values in the following experiments, the values of all gravitational curvature components of the tesseroid and spherical shell should be divided by $G\rho R_0^2$. Because the term $G\rho R_0^2$ with the unit $m^3\ kg^{-1}\ s^{-2} \times kg\ m^{-3} \times m^2 = m^2\ s^{-2}$ is omitted when calculating gravitational curvature of the tesseroid using the Fortran codes `xtessgc.f90` and `xqtessgc.f90` in Appendix C. The unit for the calculated values of gravitational curvature components of the tesseroid and spherical shell is m^{-3}. In other words, the unit of the absolute errors and Laplace's equation parameters in Eqs. (48–50) is m^{-3}.

3.2 Investigation on the computation time of gravitational potential, gravitational vector, gravitational gradient tensor , and gravitational curvature

The computation efficiency of gravitational curvature components is an essential factor that must be considered when applying gravitational curvature components for large-scale and high-resolution practical applications. The computation time of gravitational curvature is investigated in this section to demonstrate its computation efficiency. According to Eqs. (35–44), the gravitational curvature is evaluated using the numerical results of gravitational potential, gravitational vector, and gravitational gradient tensor. In other words, the outputs of gravitational potential, gravitational vector, and gravitational gradient tensor of the tesseroid are the inputs of gravitational curvature; see also Fig. 9 of Appendix C. To demonstrate the overall numerical efficiency, we also include the computation time of gravitational potential, gravitational vector, and gravitational gradient tensor. Regarding the numerical strategy, a spherical shell is discretized into the tesseroids using different grid sizes.

The basic information about the spherical shell is shown in Table 2. The spherical latitude, longitude, and height of the single computation point are $\Phi = 0°$, $\Lambda = 180°$, and $H = 100$ km, respectively. The grid size of the discretized tesseroids is chosen from $30° \times 30°$ to $5' \times 5'$ in the spherical latitudinal and longitudinal directions as $\Delta\Phi \times \Delta\Lambda$. The evaluation is performed on a desktop computer with an Intel CPU i5-10400 at 2.9 GHz, 32 GB RAM, and 1 TB SSD using single-threaded operation. The unit of computation time is second.

The numerical values of the computation time of gravitational potential, gravitational vector, gravitational gradient tensor , and gravitational curvature of the discretized tesseroids with different grid sizes in double precision are listed in Table 3. Generally, Table 3 shows that the computation time gets larger with finer grid sizes of the tesseroid. Regarding the grid size of $5' \times 5'$ with 9 331 200 tesseroids for a single computation point, the total computation time of gravitational potential, gravitational vector, gravitational gradient tensor, and gravitational curvature is about 535 083.33 / $(3600 \times 24) \approx 6.2$ days, in which the computation times of gravitational potential, gravitational vector, gravitational gradient tensor, and gravitational curvature are approximately 6 607.64 / 3600 $\approx$ 1.8 hours, 39 642.18 / 3600 $\approx$ 11.0 hours, 118 931.84 / $(3600 \times 24) \approx 1.4$ days, and 369 901.67 / $(3600 \times 24) \approx 4.3$ days, respectively.

The average value of the total computation time of gravitational potential, gravitational vector, gravitational gradient tensor , and gravitational curvature is 0.06 s for a single computation point with each single tesseroid, where the average computation time of gravitational gradient tensor and gravitational curvature is 0.01 s and 0.04 s with the ratios of 1/6 and 2/3. Regarding the internal comparison of the computation time, the average values of the computation time of gravitational vector (GV), gravitational gradient tensor (GGT), and gravitational curvature (GC) divided by the computation time of gravitational potential (GP) are 6.29 for the GV/GP, 19.20 for the GGT/GP, and 59.15 for the GC/GP, respectively.

When selecting the grid size of the tesseroid in the specific calculation, these values of the computation time in Table 3 can be used as the basic parameters by multiplying the numbers of the computation points and the tesseroids to obtain the total computation time of gravitational potential, gravitational vector, gravitational gradient tensor, and gravitational curvature.

3.3 The influence of the height on gravitational curvature

Regarding the previous studies on gravitational curvature of the tesseroid using different numerical approaches (Deng and Shen 2018a, b, 2019), there exists the near-zone problem that has significant errors when the computation point approaches the surface of the spherical shell with the discretized tesseroids. In this section, the numerical techniques

Table 3 Computation time of gravitational potential, gravitational vector, gravitational gradient tensor , and gravitational curvature with different grid sizes in double precision

Grid size	N	GP	GV	GGT	GC	All	GP/N	GV/N	GGT/N	GC/N	All/N	GV/GP	GGT/GP	GC/GP
30° × 30°	72	0.05	0.40	1.32	3.84	5.62	0.00	0.01	0.02	0.05	0.08	8.00	26.40	76.8
20° × 20°	162	0.14	0.88	2.72	8.32	12.05	0.00	0.01	0.02	0.05	0.07	6.29	19.43	59.43
18° × 18°	200	0.16	1.06	3.33	10.10	14.65	0.00	0.01	0.02	0.05	0.07	6.63	20.81	63.13
15° × 15°	288	0.22	1.39	4.36	13.58	19.54	0.00	0.00	0.02	0.05	0.07	6.32	19.82	61.73
12° × 12°	450	0.34	2.13	6.48	19.97	28.91	0.00	0.00	0.01	0.04	0.06	6.26	19.06	58.74
10° × 10°	648	0.46	2.91	8.83	27.43	39.63	0.00	0.00	0.01	0.04	0.06	6.33	19.20	59.63
9° × 9°	800	0.57	3.60	11.05	34.17	49.39	0.00	0.00	0.01	0.04	0.06	6.32	19.39	59.95
6° × 6°	1 800	1.28	7.87	23.96	74.29	107.39	0.00	0.00	0.01	0.04	0.06	6.15	18.72	58.04
5° × 5°	2 592	1.85	11.49	34.38	106.82	154.54	0.00	0.00	0.01	0.04	0.06	6.21	18.58	57.74
4° × 4°	4 050	2.94	17.47	53.41	166.00	240.08	0.00	0.00	0.01	0.04	0.06	6.03	18.17	56.46
3° × 3°	7 200	5.11	31.46	93.50	290.80	420.87	0.00	0.00	0.01	0.04	0.06	6.16	18.30	56.91
2° × 2°	16 200	11.45	70.26	208.26	648.10	938.08	0.00	0.00	0.01	0.04	0.06	6.14	18.19	56.60
1° × 1°	64 800	45.98	276.58	832.14	2 589.12	3 743.81	0.00	0.00	0.01	0.04	0.06	6.02	18.10	56.31
30′ × 30′	259 200	183.61	1 102.87	3 312.45	10 301.17	14 900.10	0.00	0.00	0.01	0.04	0.06	6.01	18.04	56.10
15′ × 15′	1 036 800	734.64	4 408.24	13 220.71	41 145.04	59 508.63	0.00	0.00	0.01	0.04	0.06	6.00	18.00	56.01
10′ × 10′	2 332 800	1 651.88	9 916.23	29 973.45	92 520.60	134 062.16	0.00	0.00	0.01	0.04	0.06	6.00	18.15	56.01
5′ × 5′	9 331 200	6 607.64	39 642.18	118 931.84	369 901.67	535 083.33	0.00	0.00	0.01	0.04	0.06	6.00	18.00	55.98
Mean							0.00	0.00	0.01	0.04	0.06	6.29	19.20	59.15

'Grid size' means the grid size of a single tesseroid. 'N' represents the total number of the discretized tesseroids forming the whole spherical shell. 'GP', 'GV', 'GGT', and 'GC' are the total computation time for one gravitational potential component (δV), three gravitational vector components (δg_Φ, δg_Λ, and δg_H), six gravitational gradient tensor components ($\delta\Gamma_{\Phi\Phi}$, $\delta\Gamma_{\Phi\Lambda}$, $\delta\Gamma_{\Phi H}$, $\delta\Gamma_{\Lambda\Lambda}$, $\delta\Gamma_{\Lambda H}$, and $\delta\Gamma_{HH}$), and ten gravitational curvature components ($\delta G_{\Phi\Phi\Phi}$, $\delta G_{\Phi\Phi\Lambda}$, $\delta G_{\Phi\Phi H}$, $\delta G_{\Phi\Lambda H}$, $\delta G_{\Lambda\Lambda\Phi}$, $\delta G_{\Lambda\Lambda\Lambda}$, $\delta G_{\Lambda\Lambda H}$, $\delta G_{HH\Phi}$, $\delta G_{HH\Lambda}$, and δG_{HHH}). 'All' means the total values of the 'GP', 'GV', 'GGT', and 'GC'. 'GP/N', 'GV/N', 'GGT/N', 'GC/N', and 'All/N' are the values of the 'GP', 'GV', 'GGT', 'GC', and 'All' divided by the 'N', respectively. 'GV/GP', 'GGT/GP', and 'GC/GP' are the values of the 'GV', 'GGT', and 'GC' divided by the 'GP', respectively. 'Mean' represents the average values. This experiment is performed on a desktop computer with an Intel CPU i5-10400 at 2.9 GHz using single-threaded operation. The unit of computation time is second. The values are truncated to two decimal places

presented in Sect. 2.4 including conditional split, infinite difference, and double exponential rule are applied to evaluate gravitational curvature with the influence of the height of the computation point. To study the general case of the tesseroid, the situations of the computation point located inside and below the tesseroid are also included. Specifically, the relative errors, absolute errors, and Laplace's equation parameters of gravitational curvature in Eqs. (48–50) are investigated with the influence of the height of the computation point.

The numerical values of the spherical shell are presented in Table 2. The grid size of the discretized tesseroids is $30° \times 30°$. The spherical latitude and longitude of the computation point are the same as those in Sect. 3.2 as $\Phi = 0°$ and $\Lambda = 180°$. The height of the computation point is $H \in [-100\,\text{km}, -40\,\text{km})$ & $(-40\,\text{km}, 10\,\text{km})$ & $(10\,\text{km}, 100\,\text{km}]$ with an interval of 1 km. Note that the bottom and top boundaries of the spherical shell are not evaluated for the relative errors of gravitational curvature. Because these values of gravitational curvature of the spherical shell cannot be calculated based on Eqs. (45–46) unless the limit values are taken.

The absolute and relative errors in $\log_{10}$ scale of gravitational curvature components $\delta G_{\Phi\Phi H}$, $\delta G_{\Lambda\Lambda H}$, and δG_{HHH} are visualized in Fig. 1a. The absolute errors in $\log_{10}$ scale of other gravitational curvature components ($\delta G_{\Phi\Phi\Phi}$, $\delta G_{\Phi\Phi\Lambda}$, $\delta G_{\Phi\Lambda H}$, $\delta G_{\Lambda\Lambda\Phi}$, $\delta G_{\Lambda\Lambda\Lambda}$, $\delta G_{HH\Phi}$, and $\delta G_{HH\Lambda}$) and Laplace's equation parameters (δL_1, δL_2, and δL_3) are shown in Fig. 1b. Note that the unit of the absolute errors and Laplace's equation parameters is m^{-3}.

In Fig. 1a, the relative errors in $\log_{10}$ scale of gravitational curvature component δG_{HHH} around the bottom and top boundaries (i.e. $H_B = -40$ km and $H_T = 10$ km) of the spherical shell are about 2 at $H = -38$ km, 2 at $H = 8$ km, and 4 at $H = 12$ km. The absolute error in $\log_{10}$ scale of the δG_{HHH} is about -8 at $H = -42$ km. These values are the large errors, which belong to the numerical outliers. Except for these outliers, the ranges of the absolute errors in $\log_{10}$ scale of gravitational curvature components $\delta G_{\Phi\Phi H}$, $\delta G_{\Lambda\Lambda H}$, and δG_{HHH} are about $[-19, -16]$ in the height of $[-100\,\text{km}, -40\,\text{km})$ and the relative errors in $\log_{10}$ scale are about $[-8, -4]$ in the heights of $(-40\,\text{km}, 10\,\text{km})$ and $(10\,\text{km}, 100\,\text{km}]$. Thus, the numerical values of the relative errors of gravitational curvature components $\delta G_{\Phi\Phi H}$, $\delta G_{\Lambda\Lambda H}$, and δG_{HHH} can provide the proper numerical precision.

In Fig. 1b, the absolute errors in $\log_{10}$ scale are mostly in the range of $[-28, -16]$ for other gravitational curvature components ($\delta G_{\Phi\Phi\Phi}$, $\delta G_{\Phi\Phi\Lambda}$, $\delta G_{\Phi\Lambda H}$, $\delta G_{\Lambda\Lambda\Phi}$, $\delta G_{\Lambda\Lambda\Lambda}$, $\delta G_{HH\Phi}$, and $\delta G_{HH\Lambda}$) and Laplace's equation parameters (δL_1, δL_2, and δL_3). Regarding the absolute errors in Fig. 1a and b, they are less than or equal to 10^{-16}, which is the chosen double precision environment in this study. In other words, the calculated absolute errors satisfy the chosen double precision.

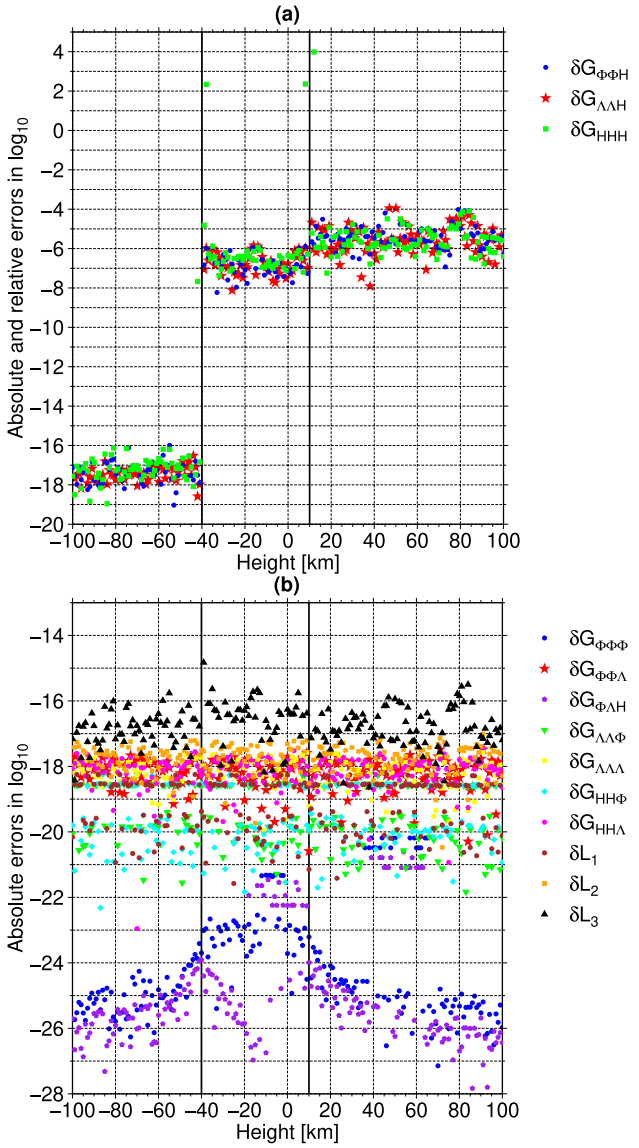

Fig. 1 **a** Visualization of the absolute errors in $[-100\,\text{km}, -40\,\text{km})$ and relative errors in $(-40\,\text{km}, +10\,\text{km})$ and $(+10\,\text{km}, +100\,\text{km}]$ in $\log_{10}$ scale of the $\delta G_{\Phi\Phi H}$ with blue circle points, $\delta G_{\Lambda\Lambda H}$ with red star points, and δG_{HHH} with green square points with the influence of the height H from -100 km to $+100$ km with an interval of 1 km; **b** the absolute errors in $\log_{10}$ scale of the $\delta G_{\Phi\Phi\Phi}$ with blue circle points, $\delta G_{\Phi\Phi\Lambda}$ with red star points, $\delta G_{\Phi\Lambda H}$ with purple pentagon points, $\delta G_{\Lambda\Lambda\Phi}$ with green inverted triangle points, $\delta G_{\Lambda\Lambda\Lambda}$ with yellow square points, $\delta G_{HH\Phi}$ with cyan diamond points, $\delta G_{HH\Lambda}$ with magenta hexagon points, δL_1 with brown octagon points, δL_2 with orange cross points, and δL_3 with black triangle points. The bottom and top boundaries of the spherical shell are at $H_B = -40$ km and $H_T = +10$ km denoted by two solid vertical lines. The grid size of the discretized tesseroids is $30° \times 30°$

In Fig. 1, the near-zone transitions between the spherical shell and its inner or outer space are interesting. The smaller height interval of 0.02 km is adopted for the near-zone as the height within $[+9$ km, $+10$ km) and $(+10$ km, $+11$ km]. The numerical results are presented in Fig. 2. The

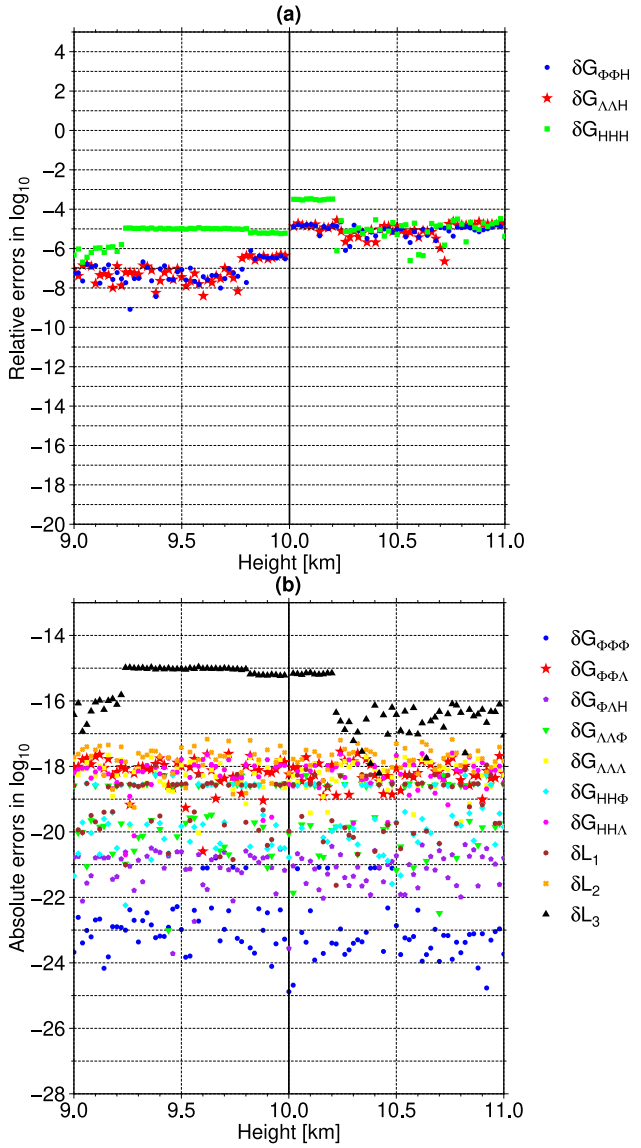

Fig. 2 **a** Visualization of the relative errors in $\log_{10}$ scale of gravitational curvature with the influence of the height H in [+9 km, +10 km) and (+10 km, +11 km] with an interval of 0.02 km; **b** the absolute errors in $\log_{10}$ scale of gravitational curvature and Laplace's equation parameters. Other parameters are the same as in Fig. 1

relative errors of gravitational curvature in Fig. 2a are in the range of $[-9, -4]$. The absolute errors and Laplace's equation parameters of gravitational curvature in Fig. 2b are about within $[-25, -15]$. Numerical results reveal that the near-zone problem for gravitational curvature of the tesseroid can be solved using the proposed approach in this study.

The numerical results in Figs. 1 and 2 reveal that the calculated values of gravitational curvature are enough to provide the proper precision for the tesseroid in practical applications based on their relative and absolute errors with respect to the reference values of the spherical shell.

3.4 Grid size effect for the influence of the height on gravitational curvature

In the previous study, Deng and Shen (2019) studied the effects of the number of discretized tesseroids on the evaluation of gravitational curvature using the distance-size ratio values. Generally, the accuracy of gravitational curvature becomes better with the increased number of discretized tesseroids (i.e., finer grid sizes), which is called the grid size refinement effect. In addition, the corresponding computation time will increase. In this study, we investigate the effects of the grid size on the near-zone problem and whether the calculated values of gravitational curvature near the bottom and top boundaries of the spherical shell would vary with different grid sizes.

This section is an extension of Sect. 3.3, i.e. the numerical settings are the same as those in Sect. 3.3. The only difference lies in the grid size of the discretized tesseroids. The chosen grid sizes in this section are $20^\circ \times 20^\circ$, $10^\circ \times 10^\circ$, $5^\circ \times 5^\circ$, and $1^\circ \times 1^\circ$, which are finer than $30^\circ \times 30^\circ$ in Sect. 3.3.

The absolute and relative errors in $\log_{10}$ scale of gravitational curvature components $\delta G_{\Phi\Phi H}$, $\delta G_{\Lambda\Lambda H}$, and δG_{HHH} using different grid sizes are shown in Fig. 3. The absolute errors in $\log_{10}$ scale of other gravitational curvature components and Laplace's equation parameters are shown in Fig. 4 with different grid sizes. To quantify the numerical results of the effects of the grid size, the statistical values, including the minimum (Min), maximum (Max), and mean values (Mean), are listed in Table 4 for the relative errors in $\log_{10}$ scale, Table 5 for the absolute errors in $\log_{10}$ scale, and Table 6 for Laplace's equation parameters in $\log_{10}$ scale, respectively. The statistical values of the grid size $30^\circ \times 30^\circ$ in Fig. 1 are also included.

In Fig. 3a, it can be clearly seen that the relative errors in $\log_{10}$ scale of the δG_{HHH} are about 3 at $H = -39$ km, 3 at $H = 9$ km, and 5 at $H = 11$ km and the absolute error in $\log_{10}$ scale of the δG_{HHH} is about -7 at $H = -41$ km for the grid size $20^\circ \times 20^\circ$ in Fig. 3a, which belong to the numerical outliers. Whereas at other heights based on Tables 4 and 5, the relative and absolute errors in $\log_{10}$ scale of the δG_{HHH} are in the range of about $[-9, -4]$ and $[-19, -16]$, which are at the acceptable precision levels as -6.4 and -16 based on Eq. (34) of this study. For the δG_{HHH} in Figs. 3b–d, there are no numerical outliers for the relative and absolute errors. Moreover, the numerical outliers are not found for the relative and absolute errors in $\log_{10}$ scale of the $\delta G_{\Phi\Phi H}$ and $\delta G_{\Lambda\Lambda H}$ in Fig. 3a–d.

The absolute errors and Laplace's equation parameters in Fig. 4 are approximately smaller than or equal to 10^{-16} with different grid sizes, indicating that these errors are round-off

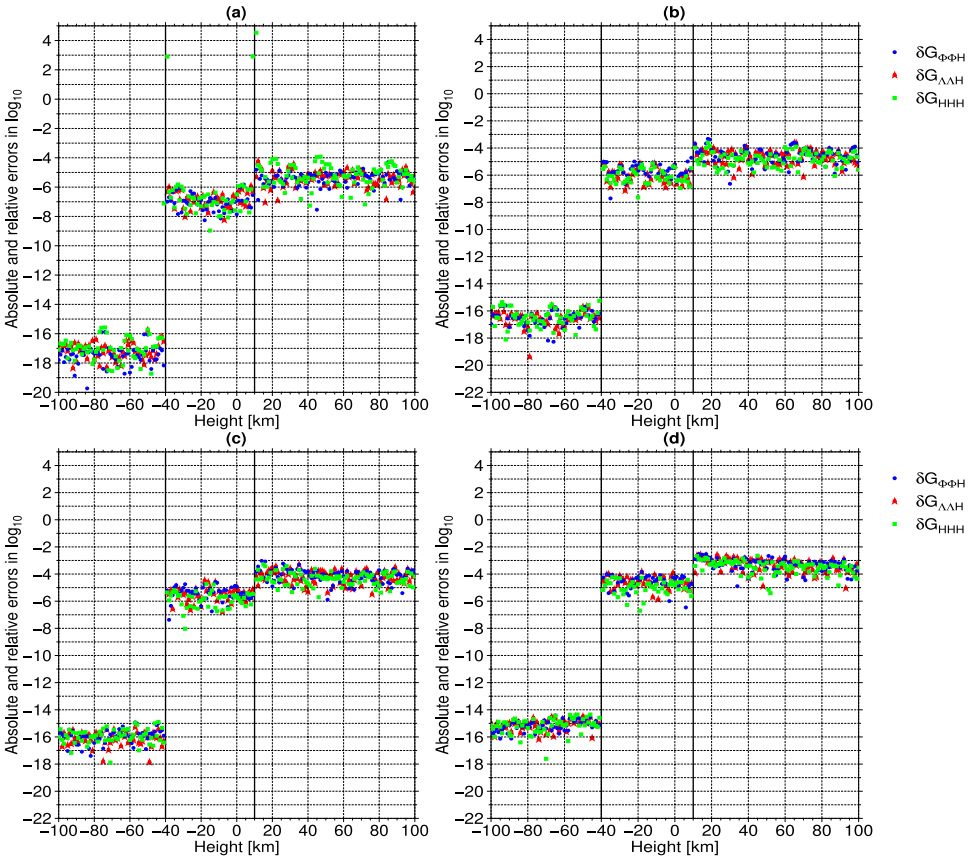

Fig. 3 Visualization of the absolute and relative errors in $\log_{10}$ scale of gravitational curvature components ($\delta G_{\Phi\Phi H}$, $\delta G_{\Lambda\Lambda H}$, and δG_{HHH}) by grid sizes of **a** 20° × 20°, **b** 10° × 10°, **c** 5° × 5°, and **d** 1° × 1°. Other parameters are the same as in Fig. 1a

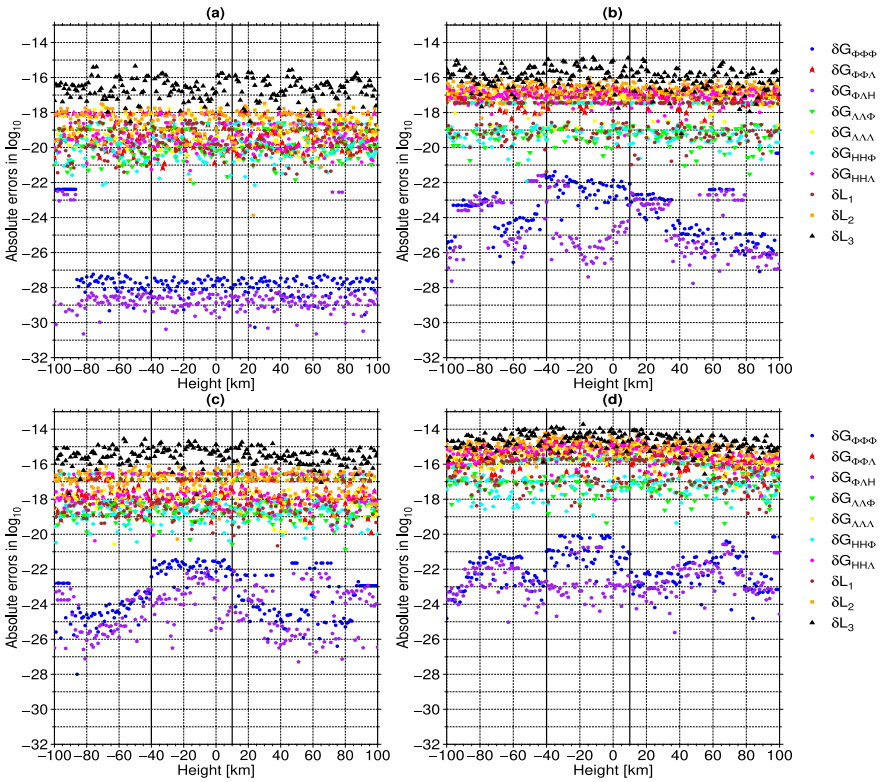

Fig. 4 Visualization of the absolute errors in $\log_{10}$ scale of gravitational curvature components ($\delta G_{\Phi\Phi\Phi}$, $\delta G_{\Phi\Phi\Lambda}$, $\delta G_{\Phi\Lambda H}$, $\delta G_{\Lambda\Lambda\Phi}$, $\delta G_{\Lambda\Lambda\Lambda}$, $\delta G_{HH\Phi}$, and $\delta G_{HH\Lambda}$) and Laplace's equation parameters (δL_1, δL_2, and δL_3) by grid sizes of **a** 20° × 20°, **b** 10° × 10°, **c** 5° × 5°, and **d** 1° × 1°. Other parameters are the same as in Fig. 1b

Table 4 Statistical values of the relative errors in $\log_{10}$ scale in Figs. 1a and 3 removing the outliers near the boundaries of the spherical shell, where the Min, Max, and Mean are the values of the minimum, maximum, and mean

Grid size	Quantity	Min	Max	Mean
30° × 30° in Fig. 1a	$\delta G_{\Phi\Phi H}$	−8.2	−4.0	−5.9
	$\delta G_{\Lambda\Lambda H}$	−8.1	−3.9	−6.0
	δG_{HHH}	−7.4	−4.1	−5.9
20° × 20° in Fig. 3a	$\delta G_{\Phi\Phi H}$	−8.3	−4.3	−6.0
	$\delta G_{\Lambda\Lambda H}$	−8.2	−4.2	−5.9
	δG_{HHH}	−9.0	−3.9	−5.8
10° × 10° in Fig. 3b	$\delta G_{\Phi\Phi H}$	−7.7	−3.3	−5.0
	$\delta G_{\Lambda\Lambda H}$	−7.1	−3.6	−5.1
	δG_{HHH}	−7.6	−3.6	−5.3
5° × 5° in Fig. 3c	$\delta G_{\Phi\Phi H}$	−7.4	−3.0	−4.6
	$\delta G_{\Lambda\Lambda H}$	−6.8	−3.3	−4.7
	δG_{HHH}	−8.0	−3.3	−4.9
1° × 1° in Fig. 3d	$\delta G_{\Phi\Phi H}$	−6.5	−2.5	−3.8
	$\delta G_{\Lambda\Lambda H}$	−5.9	−2.6	−3.8
	δG_{HHH}	−6.7	−2.7	−4.0

The values are truncated to one decimal place

errors of the computer and they satisfy the chosen double precision 10^{-16}.

Based on the numerical values in Tables 4 and 6, with the finer grid size, the mean values of the relative errors in $\log_{10}$ scale of the $\delta G_{\Lambda\Lambda H}$ and δG_{HHH} and the absolute errors in $\log_{10}$ scale of the δL_3 increase. For instance, the mean values of the relative errors in $\log_{10}$ scale of the $\delta G_{\Lambda\Lambda H}$ are approximately −6.0 for the 30° × 30°, −5.9 for the 20° × 20°, −5.1 for the 10° × 10°, −4.7 for the 5° × 5°, and −3.8 for the 1° × 1°, respectively. The mean values of the absolute errors in $\log_{10}$ scale of the δL_3 are about −16.8 for the 30° × 30°, −16.7 for the 20° × 20°, −16.0 for the 10° × 10°, −15.5 for the 5° × 5°, and −14.6 for the 1° × 1°, respectively. This may be the reason that the superposition error effect is greater than the grid size refinement effect. Specifically, each single tesseroid has a small error caused by the applied numerical techniques, e.g., the truncated Taylor series expansion and double exponential rule. Thus, the sum of each single tesseroid has more significant errors than each single tesseroid. When the number of discretized tesseroids increases, the errors also increase. This superposition error effect due to the applied numerical approach will be investigated carefully in future studies.

In short, all relative and absolute errors in Figs. 1, 2, 3, and 4 do not change significantly or can be within suitable and acceptable ranges when the computation point goes from far to near zone of the spherical shell or discretized tesseroids. Thus, the near-zone problem for gravitational curvature of

Table 5 Statistical values of the absolute errors in $\log_{10}$ scale in Figs. 1b and 4 removing the outliers near the boundaries of the spherical shell

Grid size	Quantity	Min	Max	Mean
30° × 30° in Fig. 1b	$\delta G_{\Phi\Phi H}$	−19.0	−16.0	−17.4
	$\delta G_{\Lambda\Lambda H}$	−18.6	−16.5	−17.5
	δG_{HHH}	−19.0	−16.1	−17.2
	$\delta G_{\Phi\Phi\Phi}$	−27.1	−20.2	−24.2
	$\delta G_{\Phi\Phi\Lambda}$	−20.6	−17.5	−18.2
	$\delta G_{\Phi\Lambda H}$	−27.8	−20.6	−24.9
	$\delta G_{\Lambda\Lambda\Phi}$	−21.8	−18.2	−19.4
	$\delta G_{\Lambda\Lambda\Lambda}$	−20.0	−17.6	−18.2
	$\delta G_{HH\Phi}$	−22.3	−18.2	−19.6
	$\delta G_{HH\Lambda}$	−23.0	−17.4	−18.2
20° × 20° in Fig. 4a	$\delta G_{\Phi\Phi H}$	−19.7	−15.9	−17.5
	$\delta G_{\Lambda\Lambda H}$	−18.3	−15.8	−17.2
	δG_{HHH}	−18.7	−15.6	−17.0
	$\delta G_{\Phi\Phi\Phi}$	−30.3	−22.4	−27.5
	$\delta G_{\Phi\Phi\Lambda}$	−21.2	−18.0	−19.2
	$\delta G_{\Phi\Lambda H}$	−31.1	−22.5	−28.6
	$\delta G_{\Lambda\Lambda\Phi}$	−22.0	−18.6	−19.8
	$\delta G_{\Lambda\Lambda\Lambda}$	−21.0	−17.6	−18.9
	$\delta G_{HH\Phi}$	−22.1	−18.6	−19.8
	$\delta G_{HH\Lambda}$	−21.3	−18.0	−19.3
10° × 10° in Fig. 4b	$\delta G_{\Phi\Phi H}$	−18.3	−15.6	−16.5
	$\delta G_{\Lambda\Lambda H}$	−19.4	−15.6	−16.5
	δG_{HHH}	−18.1	−15.3	−16.5
	$\delta G_{\Phi\Phi\Phi}$	−27.1	−20.3	−23.7
	$\delta G_{\Phi\Phi\Lambda}$	−19.9	−16.4	−17.1
	$\delta G_{\Phi\Lambda H}$	−27.8	−21.6	−24.6
	$\delta G_{\Lambda\Lambda\Phi}$	−21.5	−17.1	−18.7
	$\delta G_{\Lambda\Lambda\Lambda}$	−19.4	−16.5	−17.2
	$\delta G_{HH\Phi}$	−21.9	−17.1	−18.6
	$\delta G_{HH\Lambda}$	−19.3	−16.5	−17.1
5° × 5° in Fig. 4c	$\delta G_{\Phi\Phi H}$	−17.4	−14.9	−16.0
	$\delta G_{\Lambda\Lambda H}$	−17.9	−15.3	−16.1
	δG_{HHH}	−17.9	−14.9	−15.9
	$\delta G_{\Phi\Phi\Phi}$	−28.0	−21.4	−23.5
	$\delta G_{\Phi\Phi\Lambda}$	−19.9	−16.5	−17.7
	$\delta G_{\Phi\Lambda H}$	−28.2	−22.1	−24.4
	$\delta G_{\Lambda\Lambda\Phi}$	−20.9	−16.5	−18.1
	$\delta G_{\Lambda\Lambda\Lambda}$	−20.6	−16.1	−17.4
	$\delta G_{HH\Phi}$	−20.5	−16.5	−18.3
	$\delta G_{HH\Lambda}$	−20.1	−16.5	−17.6
1° × 1° in Fig. 4d	$\delta G_{\Phi\Phi H}$	−16.1	−14.4	−15.2
	$\delta G_{\Lambda\Lambda H}$	−16.2	−14.5	−15.1
	δG_{HHH}	−17.6	−14.3	−15.2
	$\delta G_{\Phi\Phi\Phi}$	−24.8	−20.1	−22.0
	$\delta G_{\Phi\Phi\Lambda}$	−17.8	−14.5	−15.5
	$\delta G_{\Phi\Lambda H}$	−25.6	−20.4	−22.7

Table 5 continued

Grid size	Quantity	Min	Max	Mean
	$\delta G_{\Lambda\Lambda\Phi}$	−19.4	−15.4	−16.7
	$\delta G_{\Lambda\Lambda\Lambda}$	−17.7	−14.7	−15.6
	$\delta G_{HH\Phi}$	−19.4	−15.4	−16.9
	$\delta G_{HH\Lambda}$	−18.0	−14.6	−15.5

Other parameters are the same as those in Table 4

Table 6 Statistical values of the Laplace's equation parameters in $\log_{10}$ scale in Figs. 1b and 4 removing the outliers near the boundaries of the spherical shell

Grid size	Quantity	Min	Max	Mean
30° × 30° in Fig. 1b	δL_1	−21.6	−18.1	−19.2
	δL_2	−20.5	−17.0	−17.8
	δL_3	−18.6	−14.8	−16.8
20° × 20° in Fig. 4a	δL_1	−21.5	−18.4	−19.6
	δL_2	−23.9	−17.5	−18.6
	δL_3	−18.5	−15.3	−16.7
10° × 10° in Fig. 4b	δL_1	−21.4	−17.0	−18.5
	δL_2	−18.9	−16.0	−16.7
	δL_3	−19.2	−14.8	−16.0
5° × 5° in Fig. 4c	δL_1	−20.7	−16.3	−17.9
	δL_2	−20.3	−16.0	−17.0
	δL_3	−17.7	−14.6	−15.5
1° × 1° in Fig. 4d	δL_1	−18.8	−15.2	−16.6
	δL_2	−17.6	−14.2	−15.1
	δL_3	−16.6	−13.7	−14.7

Other parameters are the same as those in Table 4

the tesseroid could be adequately solved using the proposed numerical approach in Sect. 2.4.

3.5 The influence of the latitude on gravitational curvature

Previous studies revealed that the geometry of the tesseroid affected the relative errors of gravitational curvature at the satellite height, i.e., the relative errors increased especially near the polar region (Deng and Shen 2018a, b). In this section, we apply the numerical approach presented in Sect. 2.4 to investigate whether the evaluation of gravitational curvature varies with the geometry of the tesseroid near the polar region, i.e., polar-region problem. Specifically, the influence of the latitude of the computation point on gravitational curvature is performed using the spherical shell discretized into tesseroids. In addition, the polar-singularity problem, i.e., there are numerical outliers at the polar points, is investigated with the numerical approach in Sect. 2.4. The relative errors of gravitational potential (δV), gravitational vector (δg_H), and gravitational gradient tensor ($\delta\Gamma_{\Phi\Phi}$, $\delta\Gamma_{\Lambda\Lambda}$, and $\delta\Gamma_{HH}$) are included as comparisons to those of gravitational curvature. The calculation of the relative errors of gravitational potential, gravitational vector, and gravitational gradient tensor components can be referred to in Sect. 3.1 of Fukushima (2018) and Sect. 4 of Deng (2023a).

Similarly, the numerical values of the spherical shell are listed in Table 2. Due to the spherical symmetry of the northern and southern hemispheres of the spherical shell, the spherical latitude of the computation point is $\Phi \in [0°, 90°]$ with an interval of 1°. The spherical longitude of the computation point is $\Lambda = 0°$. The height of the computation point is $H = 260$ km, which was usually adopted as the GOCE (Gravity Field and Steady-State Ocean Circulation Explorer, Rummel et al. (2011)) satellite height. This height is the same as that in Deng and Shen (2018a), Deng and Shen (2018b), and Deng (2023b). The grid size of the discretized tesseroids is 30° × 30°.

The relative errors in $\log_{10}$ scale of gravitational potential (δV), gravitational vector (δg_H), gravitational gradient tensor ($\delta\Gamma_{\Phi\Phi}$, $\delta\Gamma_{\Lambda\Lambda}$, and $\delta\Gamma_{HH}$), and gravitational curvature ($\delta G_{\Phi\Phi H}$, $\delta G_{\Lambda\Lambda H}$, and δG_{HHH}) with the influence of the latitude are illustrated in Fig. 5a. In addition, the absolute errors ($\delta G_{\Phi\Phi\Phi}$, $\delta G_{\Phi\Phi\Lambda}$, $\delta G_{\Phi\Lambda H}$, $\delta G_{\Lambda\Lambda\Phi}$, $\delta G_{\Lambda\Lambda\Lambda}$, $\delta G_{HH\Phi}$, and $\delta G_{HH\Lambda}$) and Laplace's equation parameters (δL_1, δL_2, and δL_3) in $\log_{10}$ scale of gravitational curvature are shown in Fig. 5b.

In Fig. 5a, it can be clearly found that there are two numerical outliers for gravitational gradient tensor component $\delta\Gamma_{\Lambda\Lambda}$ and gravitational curvature component $\delta G_{\Lambda\Lambda H}$ at the latitude $\Phi = 90°$. In detail, the relative errors in $\log_{10}$ scale are about 5 for the $\delta\Gamma_{\Lambda\Lambda}$ and 8 for the $\delta G_{\Lambda\Lambda H}$ at the polar point $\Phi = 90°$. Similarly, at the latitude $\Phi = 90°$ in Fig. 5b, the numerical outliers exist for these gravitational curvature components (i.e., $\delta G_{\Phi\Phi\Lambda}$, $\delta G_{\Phi\Lambda H}$, $\delta G_{\Lambda\Lambda\Phi}$, $\delta G_{\Lambda\Lambda\Lambda}$, and $\delta G_{HH\Lambda}$) and Laplace's equation parameters (i.e. δL_1, δL_2, and δL_3). The absolute errors in $\log_{10}$ scale are approximately 8 for the $\delta G_{\Phi\Phi\Lambda}$, $\delta G_{\Lambda\Lambda\Lambda}$; 3 for the $\delta G_{\Phi\Lambda H}$; 9 for the $\delta G_{\Lambda\Lambda\Phi}$, δL_1; −13 for the $\delta G_{HH\Lambda}$; 2 for the δL_2; and −4 for the δL_3, respectively.

In Fig. 5a, except for the abnormal values at the latitude 90°, the relative errors of gravitational potential, gravitational vector, gravitational gradient tensor, and gravitational curvature do not increase with the increased latitude. These relative errors show the irregular discrete distribution. Thus, the polar-region problem for gravitational curvature of the tesseroid can be solved using the numerical approach in this study. Specifically, the relative errors in $\log_{10}$ scale are in the range of about [−16, −15] for gravitational potential (δV), [−13, −10] for gravitational vector (δg_H), [−9, −6] for gravitational gradient tensor ($\delta\Gamma_{\Phi\Phi}$, $\delta\Gamma_{\Lambda\Lambda}$, and $\delta\Gamma_{HH}$), and [−8, −4] for gravitational curvature ($\delta G_{\Phi\Phi H}$, $\delta G_{\Lambda\Lambda H}$, and δG_{HHH}), respectively.

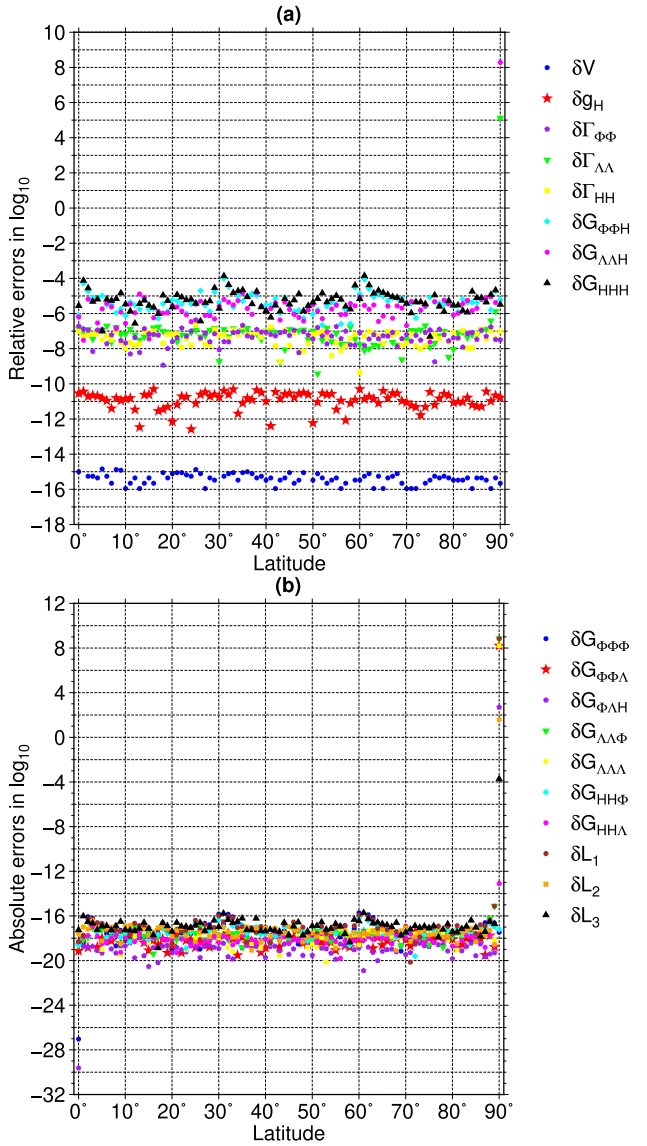

Fig. 5 **a** Illustration of the relative errors in $\log_{10}$ scale of the δV with blue circle points, δg_H with red star points, $\delta\Gamma_{\Phi\Phi}$ with purple pentagon points, $\delta\Gamma_{\Lambda\Lambda}$ with green inverted triangle points, $\delta\Gamma_{HH}$ with yellow square triangle points, $\mathrm{G}_{\Phi\Phi H}$ with cyan diamond points, $\delta\mathrm{G}_{\Lambda\Lambda H}$ with magenta hexagon points, and $\delta\mathrm{G}_{HHH}$ with black triangle points with the influence of the latitude of the computation point from 0° to 90° with an interval of 1° at the satellite height of 260 km; **b** the absolute errors in $\log_{10}$ scale of gravitational curvature components ($\delta\mathrm{G}_{\Phi\Phi\Phi}$, $\delta\mathrm{G}_{\Phi\Phi\Lambda}$, $\delta\mathrm{G}_{\Phi\Lambda H}$, $\delta\mathrm{G}_{\Lambda\Lambda\Phi}$, $\delta\mathrm{G}_{\Lambda\Lambda\Lambda}$, $\delta\mathrm{G}_{HH\Phi}$, and $\delta\mathrm{G}_{HH\Lambda}$) and their Laplace's equation parameters (δL_1, δL_2, and δL_3). Other parameters are the same as in Fig. 1b

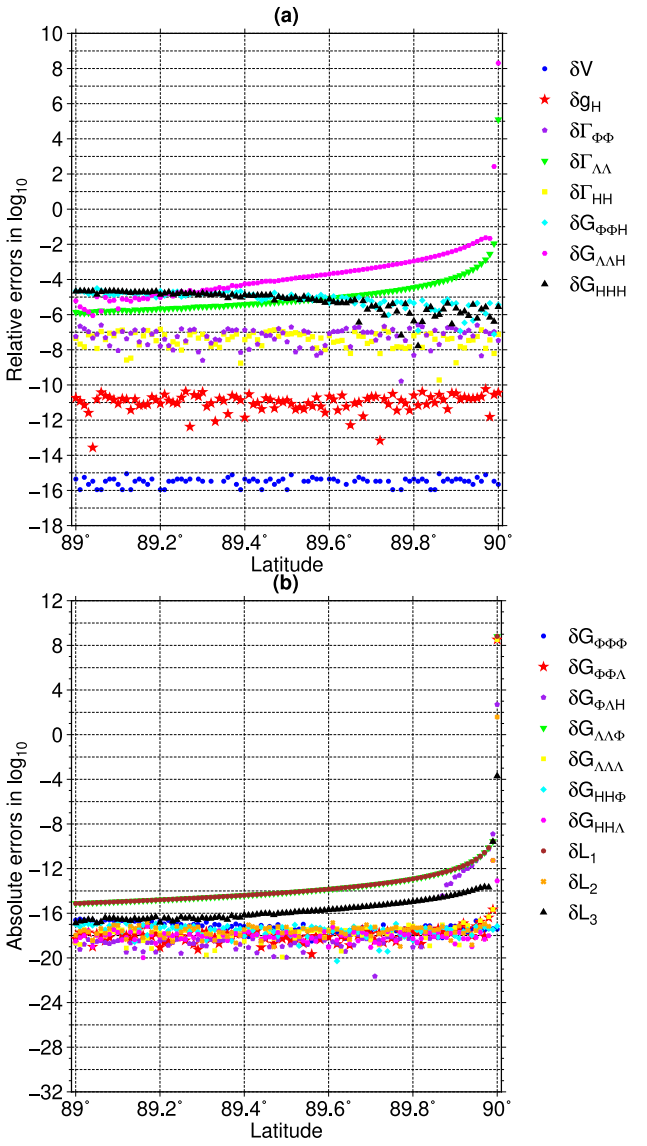

Fig. 6 **a** Illustration of the relative errors in $\log_{10}$ scale of the δV, δg_H, $\delta\Gamma_{\Phi\Phi}$, $\delta\Gamma_{\Lambda\Lambda}$, $\delta\Gamma_{HH}$, $\mathrm{G}_{\Phi\Phi H}$, $\delta\mathrm{G}_{\Lambda\Lambda H}$, and $\delta\mathrm{G}_{HHH}$ with the influence of the latitude of the computation point from 89° to 90° with an interval of 0.01° at the satellite height of 260 km; **b** the absolute errors in $\log_{10}$ scale of gravitational curvature components ($\delta\mathrm{G}_{\Phi\Phi\Phi}$, $\delta\mathrm{G}_{\Phi\Phi\Lambda}$, $\delta\mathrm{G}_{\Phi\Lambda H}$, $\delta\mathrm{G}_{\Lambda\Lambda\Phi}$, $\delta\mathrm{G}_{\Lambda\Lambda\Lambda}$, $\delta\mathrm{G}_{HH\Phi}$, and $\delta\mathrm{G}_{HH\Lambda}$) and their Laplace's equation parameters (δL_1, δL_2, and δL_3). Other parameters are the same as in Fig. 5

From Fig. 5b, it can be seen that these absolute errors and Laplace's equation parameters do not increase with the increased latitude. Apart from the numerical outliers at the polar point, the absolute errors in $\log_{10}$ scale of gravitational curvature components and Laplace's equation parameters are almost in the range of about $[-21, -16]$, which indicates the satisfied double precision 10^{-16}.

In Fig. 5, the instability of calculating the affected gradients near the polar singular point would be interesting. The range of the computation point's latitude is $[89°, 90°]$ with the smaller latitude interval of 0.01°. The numerical results are presented in Fig. 6. In Fig. 6, the increased relative errors are found for the $\delta\Gamma_{\Lambda\Lambda}$ and $\delta\mathrm{G}_{\Lambda\Lambda H}$ from 89.9° to 90° due to the existed polar-singularity problems for these two components, where the same situations occur for these gravitational curvature components (i.e., $\delta\mathrm{G}_{\Phi\Phi\Lambda}$, $\delta\mathrm{G}_{\Phi\Lambda H}$, $\delta\mathrm{G}_{\Lambda\Lambda\Phi}$, $\delta\mathrm{G}_{\Lambda\Lambda\Lambda}$, and $\delta\mathrm{G}_{HH\Lambda}$) and Laplace's equa-

tion parameters (i.e., δL_1, δL_2, and δL_3). Whereas the relative errors for other components of gravitational potential, gravitational vector, gravitational gradient tensor, and gravitational curvatures do not increase from 89° to 90°.

The above numerical results show that the polar-singularity problem exists for the relative errors of gravitational curvature component $\delta G_{\Lambda\Lambda H}$, the absolute errors of gravitational curvature ($\delta G_{\Phi\Phi\Lambda}$, $\delta G_{\Phi\Lambda H}$, $\delta G_{\Lambda\Lambda\Phi}$, $\delta G_{\Lambda\Lambda\Lambda}$, and $\delta G_{HH\Lambda}$), and Laplace's equation parameters (δL_1, δL_2, and δL_3) due to the numerical outliers of these parameters at the polar point $\Phi = 90°$. The reason for these outliers lies in the cos Φ in the denominator of the expressions of these components, e.g., Eqs. (36), (38–41), and (43), and Laplace's equation parameters are composed of these components.

3.6 Grid size effect for the influence of the latitude on gravitational curvature

Similar to Sect. 3.4 based on Sect. 3.3, this section investigates the grid size effect for the influence of the latitude on gravitational curvature based on Sect. 3.5. Specifically, the relative errors, absolute errors, and Laplace's equation parameters are calculated with different grid sizes based on the spherical shell discretized into tesseroids. The polar-region problem and polar-singularity problem are tested for gravitational curvature at the polar points with different grid sizes. In addition, the relative errors of gravitational potential, gravitational vector, and gravitational gradient tensor are included in comparisons with those of gravitational curvature.

Analogously, the grid size is extended from 30° × 30° to 20° × 20°, 10° × 10°, 5° × 5°, and 1° × 1°. Other numerical parameters in this section are the same as those in Sect. 3.5.

Figure 7 illustrates the relative errors in $\log_{10}$ scale of gravitational potential (δV), gravitational vector (δg_H), gravitational gradient tensor ($\delta\Gamma_{\Phi\Phi}$, $\delta\Gamma_{\Lambda\Lambda}$, and $\delta\Gamma_{HH}$), and gravitational curvature ($\delta G_{\Phi\Phi H}$, $\delta G_{\Lambda\Lambda H}$, and δG_{HHH}) with the influence of the latitude using the grid sizes 20° × 20°, 10° × 10°, 5° × 5°, and 1° × 1°. Similarly, Fig. 8 shows the absolute errors ($\delta G_{\Phi\Phi\Phi}$, $\delta G_{\Phi\Phi\Lambda}$, $\delta G_{\Phi\Lambda H}$, $\delta G_{\Lambda\Lambda\Phi}$, $\delta G_{\Lambda\Lambda\Lambda}$, $\delta G_{HH\Phi}$, and $\delta G_{HH\Lambda}$) and Laplace's equation parameters (δL_1, δL_2, and δL_3) in $\log_{10}$ scale of gravitational curvature with the different grid sizes.

In Fig. 7, there are two numerical outliers of gravitational gradient tensor component $\delta\Gamma_{\Lambda\Lambda}$ and gravitational curvature component $\delta G_{\Lambda\Lambda H}$ at the latitude $\Phi = 90°$ for different grid sizes 20° × 20°, 10° × 10°, 5° × 5°, and 1° × 1° in Fig. 7a–d, respectively. These abnormal relative errors in $\log_{10}$ scale of the $\delta\Gamma_{\Lambda\Lambda}$ and $\delta G_{\Lambda\Lambda H}$ using different grid sizes are approximately 4 and 8 for 20° × 20° in Fig. 7a; 5 and 8 for 10° × 10° in Fig. 7b; 5 and 6 for 5° × 5° in Fig. 7c; and 5 and 8 for 1° × 1° in Fig. 7d. In Fig. 8, the numerical outliers of the absolute errors in $\log_{10}$ scale for gravitational curvature components and Laplace's equation parameters at the latitude $\Phi = 90°$ using different grid sizes are listed in Table 7. Regarding the different grid sizes, there still exist the polar-singularity problems for the relative errors of gravitational curvature ($\delta G_{\Lambda\Lambda H}$), absolute errors of gravitational curvature ($\delta G_{\Phi\Phi\Lambda}$, $\delta G_{\Phi\Lambda H}$, $\delta G_{\Lambda\Lambda\Phi}$, $\delta G_{\Lambda\Lambda\Lambda}$, and $\delta G_{HH\Lambda}$), and Laplace's equation parameters (δL_1, δL_2, and δL_3).

Apart from the numerical outliers in Figs. 5, 6, 7 and 8, the statistical values of the relative errors in $\log_{10}$ scale in Figs. 5a and 7 and absolute errors in $\log_{10}$ scale in Figs. 5b and 8 are listed in Tables 8 and 9, respectively.

Based on Fig. 7 and Table 8, the ranges of the relative errors in $\log_{10}$ scale for gravitational potential (δV), gravitational vector (δg_H), gravitational gradient tensor ($\delta\Gamma_{\Phi\Phi}$, $\delta\Gamma_{\Lambda\Lambda}$, and $\delta\Gamma_{HH}$), and gravitational curvature ($\delta G_{\Phi\Phi H}$, $\delta G_{\Lambda\Lambda H}$, and δG_{HHH}) are almost at the similar level for different grid sizes by not considering the numerical outliers at the latitude $\Phi = 90°$. Similarly, removing the numerical outliers and based on Fig. 8 and Table 9, the ranges of the absolute errors in $\log_{10}$ scale of gravitational curvature components and Laplace's equation parameters are about $[-20, -16]$.

When the latitude increases in Figs. 5, 6, 7, and 8, all relative and absolute errors of gravitational curvature do not change significantly and they are within certain ranges. These numerical results with different grid sizes reveal that the geometry of the discretized tesseroids does not affect the evaluation of gravitational curvature with the influence of the latitude by using the numerical techniques of the conditional split, finite difference, and double exponential rule in this study. Thus, the polar-region problem for gravitational curvature of the tesseroid can be properly solved using the proposed numerical approach in this study.

From Tables 8 and 9, it is interesting to find that the mean values of the relative errors in $\log_{10}$ scale of gravitational potential (δV), gravitational gradient tensor ($\delta\Gamma_{\Phi\Phi}$, $\delta\Gamma_{\Lambda\Lambda}$, and $\delta\Gamma_{HH}$), and gravitational curvature ($\delta G_{\Phi\Phi H}$, $\delta G_{\Lambda\Lambda H}$, and δG_{HHH}), absolute errors in $\log_{10}$ scale of gravitational curvature ($\delta G_{\Phi\Phi\Phi}$, $\delta G_{\Phi\Phi\Lambda}$, $\delta G_{\Phi\Lambda H}$, $\delta G_{\Lambda\Lambda\Phi}$, $\delta G_{HH\Phi}$, and $\delta G_{HH\Lambda}$), and Laplace's equation parameters (δL_1, δL_2, and δL_3) increase with the finer grid sizes from 30° × 30° to 1° × 1°, excepting for the δg_H and $\delta G_{\Lambda\Lambda\Lambda}$. For example, the mean values of the relative errors in $\log_{10}$ scale of the δG_{HHH} are about −5.3, −5.2, −5.1, −4.8, and −4.7 for the grid sizes 30° × 30°, 20° × 20°, 10° × 10°, 5° × 5°, and 1° × 1°, respectively. This demonstrates the existence of the superposition error effect mentioned in Sect. 3.6 using the different grid sizes at the satellite height. Moreover, the superposition error effect of the tesseroid is larger than the grid size refinement effect for evaluating gravitational curvature of the tesseroid at the satellite height using the presented numerical approach in Sect. 2.4.

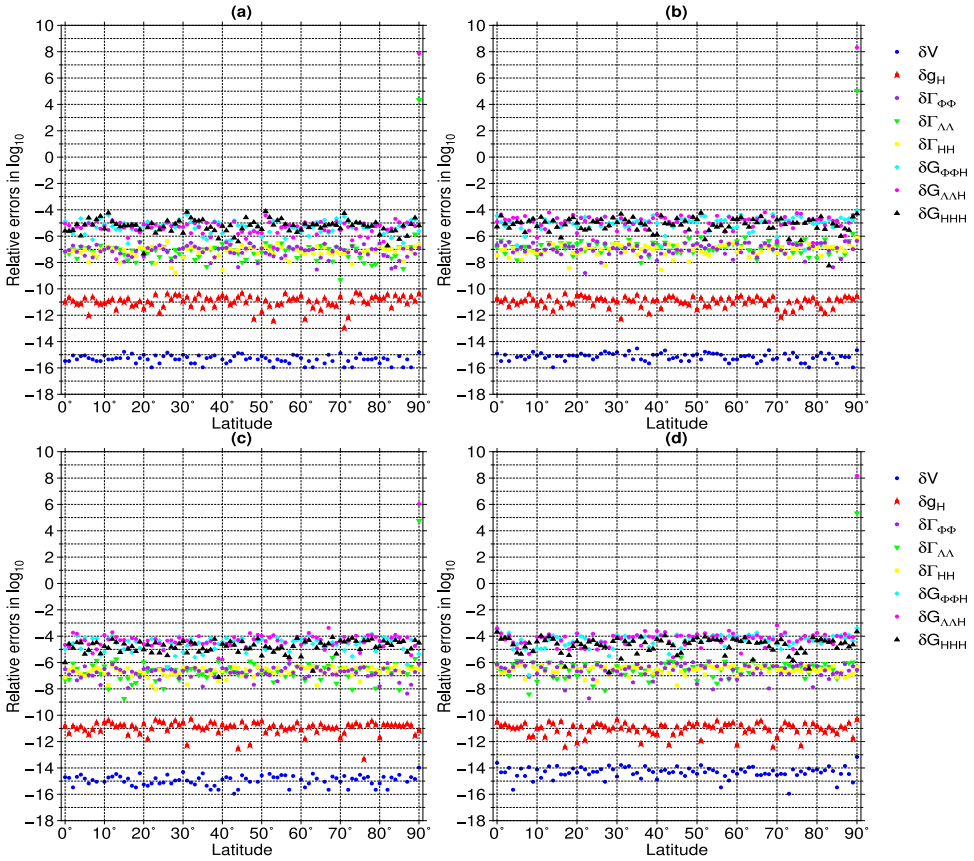

Fig. 7 Illustration of the relative errors in $\log_{10}$ scale of gravitational potential (δV), gravitational vector (δg_H), gravitational gradient tensor ($\delta\Gamma_{\Phi\Phi}$, $\delta\Gamma_{\Lambda\Lambda}$, and $\delta\Gamma_{HH}$), and gravitational curvature ($\delta G_{\Phi\Phi H}$, $\delta G_{\Lambda\Lambda H}$, and δG_{HHH}) by grid sizes of **a** 20° × 20°, **b** 10° × 10°, **c** 5° × 5°, and **d** 1° × 1°. Other parameters are the same as in Fig. 5a

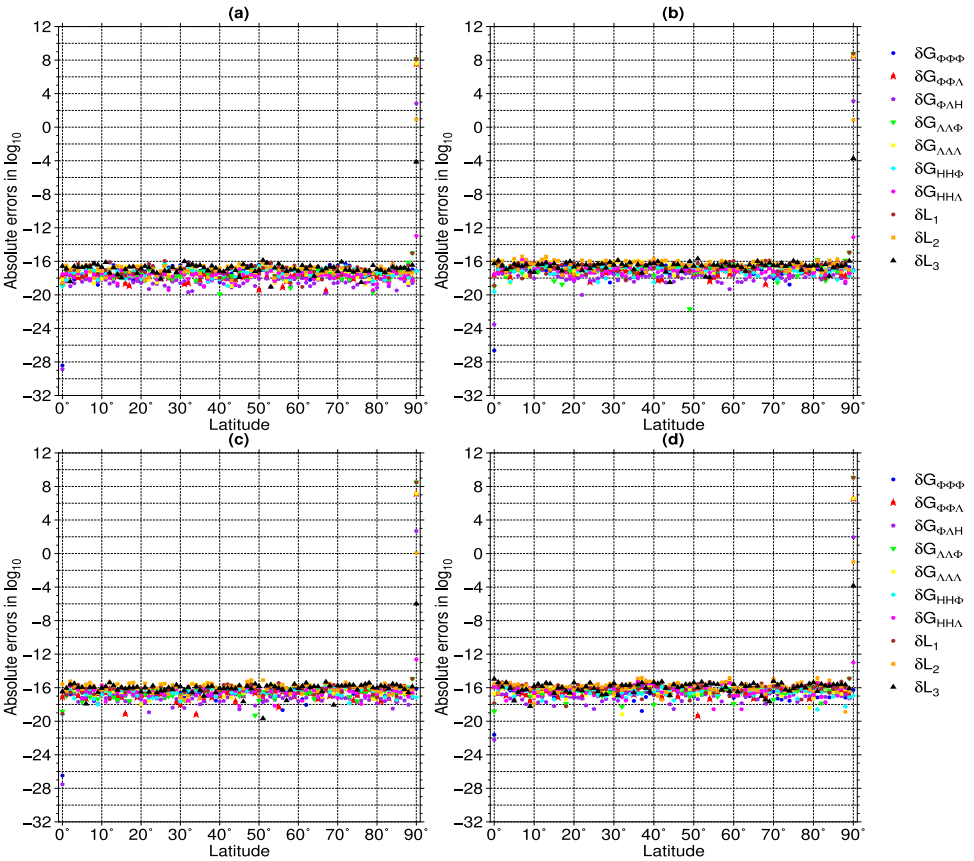

Fig. 8 Illustration of the absolute errors in $\log_{10}$ scale of gravitational curvature ($\delta G_{\Phi\Phi\Phi}$, $\delta G_{\Phi\Phi\Lambda}$, $\delta G_{\Phi\Lambda H}$, $\delta G_{\Lambda\Lambda\Phi}$, $\delta G_{\Lambda\Lambda\Lambda}$, $\delta G_{HH\Phi}$, and $\delta G_{HH\Lambda}$) and their Laplace's equation parameters (δL_1, δL_2, and δL_3) by grid sizes of **a** 20° × 20°, **b** 10° × 10°, **c** 5° × 5°, and **d** 1° × 1°. Other parameters are the same as in Fig. 5b

Table 7 Numerical outliers of the absolute errors in $\log_{10}$ scale for gravitational curvature components ($\delta G_{\Phi\Phi\Lambda}$, $\delta G_{\Phi\Lambda H}$, $\delta G_{\Lambda\Lambda\Phi}$, $\delta G_{\Lambda\Lambda\Lambda}$, and $\delta G_{HH\Lambda}$) and Laplace's equation parameters (δL_1, δL_2, and δL_3) at the latitude $\Phi = 90°$ in Fig. 8

Grid size	$\delta G_{\Phi\Phi\Lambda}$, $\delta G_{\Lambda\Lambda\Lambda}$	$\delta G_{\Phi\Lambda H}$	$\delta G_{\Lambda\Lambda\Phi}$, δL_1	$\delta G_{HH\Lambda}$	δL_2	δL_3
$20° \times 20°$ in Fig. 8a	8	3	8	−13	1	−4
$10° \times 10°$ in Fig. 8b	9	3	9	−13	1	−4
$5° \times 5°$ in Fig. 8c	7	3	8	−13	0	−6
$1° \times 1°$ in Fig. 8d	7	2	9	−13	−1	−4

Other parameters are the same as in Table 4

4 Conclusions and outlook

In this contribution, we derive new third-order central and single-sided finite formulas with one, two, and three arguments. Based on these newly derived formulas, we present a numerical approach to calculate gravitational curvature of a tesseroid, which includes the techniques of the conditional split, finite difference, and double exponential rule.

In the numerical experiments, we adopt the classical benchmark of a spherical shell discretized into tesseroids to validate the effectiveness of the proposed numerical approach. This study considers different situations of the computation point located below, inside, and above the spherical shell. In detail, the analytical solutions for gravitational curvature of a spherical shell serve as references for the discretized tesseroids.

The computation time of gravitational potential, gravitational vector, gravitational gradient tensor, and gravitational curvature with different grid sizes from $30° \times 30°$ to $5' \times 5'$ in double precision is investigated for a single computation point. Regarding the situation of a single computation point with each single tesseroid, the ratio of the average computation time for gravitational curvature is about 2/3 with respect to the mean value of the total computation time for gravitational quantities (e.g., gravitational potential, gravitational vector, gravitational gradient tensor, and gravitational curvature), where the ratio of the average computation time of gravitational gradient tensor is about 1/6.

The influence of the height of the computation point on gravitational curvature is studied using the relative errors, absolute errors, and Laplace's equation parameters in $\log_{10}$ scale with different grid sizes $30° \times 30°$, $20° \times 20°$, $10° \times 10°$, $5° \times 5°$, and $1° \times 1°$ when the computation point is located below, inside, and above the spherical shell or the discretized tesseroids. With the height increasing from below, inside, and above the spherical shell using different grid sizes, the relative errors, absolute errors, and Laplace's equation parameters of gravitational curvature do not show significant variations (c.f. the rapid drop zone in Fig. 5 of Deng and Shen (2018b)). These numerical results reveal that the near-zone problem for gravitational curvature of the tesseroid could be solved using the proposed numerical approach in this study.

Analogously, the influence of the latitude of the computation point on gravitational curvature is investigated with the same grid sizes at the satellite height of 260 km. Numerical results confirm that the polar-singularity problems exist not only for the relative errors of gravitational curvature component $\delta G_{\Lambda\Lambda H}$ but also for the absolute errors ($\delta G_{\Phi\Phi\Lambda}$, $\delta G_{\Phi\Lambda H}$, $\delta G_{\Lambda\Lambda\Phi}$, $\delta G_{\Lambda\Lambda\Lambda}$, and $\delta G_{HH\Lambda}$) and Laplace's equation parameters (δL_1, δL_2, and δL_3) of gravitational curvature at the polar point $\Phi = 90°$ with different grid sizes. The reason for the polar-singularity problem lies in the $\cos\Phi = 0$ in the denominator of the gravitational curvature expressions when $\Phi = 90°$ at the polar point. The combination of Cartesian integral kernels (Deng and Shen 2018b; Deng and Sneeuw 2023) and the numerical techniques of the conditional split, finite difference, and double exponential rule will be investigated for gravitational curvature in a future study, hoping to take advantage of avoiding the polar-singularity problem with Cartesian integral kernels and providing the proper numerical accuracy with the numerical approach proposed in this study.

Numerical experiments show that with the increased latitude, the ranges of the relative errors, absolute errors, and Laplace's equation parameters are almost at similar levels for different grid sizes. In other words, the geometry of the discretized tesseroids does not affect the evaluation of gravitational curvature by using the numerical techniques of the conditional split, finite difference, and double exponential rule in this study. Thus, the polar-region problem for gravitational curvature of the tesseroid can be properly solved because all relative and absolute errors smoothly change with the increased latitude from the equator to the north pole.

In the numerical experiments with different grid sizes on the influence of the height and latitude on gravitational curvature, with the finer grid size, the mean values of the relative errors, absolute errors, and Laplace's equation parameters in $\log_{10}$ scale of some components of gravitational curvature become larger. Generally, when the grid size gets finer (i.e., the number of discretized tesseroids becomes large), the accuracy of the evaluation of gravitational curvature is better (Deng and Shen 2019), denoted by the grid size refinement effect. In the numerical investigations of this study, the opposite numerical results are obtained, which indicate the existence of the superposition error effect, because the relative test displacement δ_3 in Eq. (33) is set for a single tesseroid. With the finer grid sizes (i.e., more discretized tesseroids are obtained), the sum of the errors of the

Table 8 Statistical values of the relative errors in $\log_{10}$ scale in Figs. 5a and 7 by removing the outliers at the latitude $\Phi = 90°$

Grid size	Quantity	Min	Max	Mean
30° × 30° in Fig. 5a	δV	−16.0	−14.8	−15.4
	δg_H	−12.6	−10.3	−10.9
	$\delta\Gamma_{\Phi\Phi}$	−8.9	−6.4	−7.3
	$\delta\Gamma_{\Lambda\Lambda}$	−9.4	−5.9	−7.3
	$\delta\Gamma_{HH}$	−9.4	−6.6	−7.4
	$\delta G_{\Phi\Phi H}$	−6.7	−4.0	−5.4
	$\delta G_{\Lambda\Lambda H}$	−7.6	−4.8	−5.8
	δG_{HHH}	−7.3	−3.8	−5.3
20° × 20° in Fig. 7a	δV	−16.0	−14.8	−15.3
	δg_H	−13.0	−10.3	−11.0
	$\delta\Gamma_{\Phi\Phi}$	−8.5	−6.4	−7.2
	$\delta\Gamma_{\Lambda\Lambda}$	−9.3	−5.9	−7.2
	$\delta\Gamma_{HH}$	−8.8	−6.4	−7.2
	$\delta G_{\Phi\Phi H}$	−6.6	−4.3	−5.3
	$\delta G_{\Lambda\Lambda H}$	−7.8	−4.4	−5.4
	δG_{HHH}	−7.3	−4.1	−5.2
10° × 10° in Fig. 7b	δV	−16.0	−14.5	−15.2
	δg_H	−12.3	−10.4	−11.0
	$\delta\Gamma_{\Phi\Phi}$	−8.8	−6.4	−7.0
	$\delta\Gamma_{\Lambda\Lambda}$	−8.0	−5.8	−6.9
	$\delta\Gamma_{HH}$	−8.5	−6.1	−7.0
	$\delta G_{\Phi\Phi H}$	−7.0	−4.1	−5.0
	$\delta G_{\Lambda\Lambda H}$	−6.5	−4.2	−4.9
	δG_{HHH}	−8.2	−4.2	−5.1
5° × 5° in Fig. 7c	δV	−16.0	−14.0	−14.9
	δg_H	−13.3	−10.3	−11.0
	$\delta\Gamma_{\Phi\Phi}$	−8.4	−6.0	−6.8
	$\delta\Gamma_{\Lambda\Lambda}$	−8.8	−5.6	−6.7
	$\delta\Gamma_{HH}$	−8.0	−6.2	−6.7
	$\delta G_{\Phi\Phi H}$	−6.4	−3.8	−4.6
	$\delta G_{\Lambda\Lambda H}$	−5.8	−3.4	−4.4
	δG_{HHH}	−7.1	−4.1	−4.8
1° × 1° in Fig. 7d	δV	−16.0	−13.2	−14.3
	δg_H	−12.4	−10.3	−11.1
	$\delta\Gamma_{\Phi\Phi}$	−8.7	−5.9	−6.6
	$\delta\Gamma_{\Lambda\Lambda}$	−8.4	−5.6	−6.5
	$\delta\Gamma_{HH}$	−7.7	−6.1	−6.6
	$\delta G_{\Phi\Phi H}$	−7.0	−3.4	−4.3
	$\delta G_{\Lambda\Lambda H}$	−5.6	−3.2	−4.2
	δG_{HHH}	−6.7	−3.7	−4.7

Other parameters are the same as in Table 4

discretized tesseroids gets larger. In other words, the superposition error effect is larger than the grid size refinement effect. It is speculated that the accuracy of the numerical evaluation of gravitational curvature of the tesseroid in this study

Table 9 Statistical values of the absolute errors and Laplace's equation parameters in $\log_{10}$ scale in Figs. 5b and 8 by removing the outliers at the latitude $\Phi = 90°$

Grid size	Quantity	Min	Max	Mean
30° × 30° in Fig. 5a	$\delta G_{\Phi\Phi\Phi}$	−27.0	−15.7	−17.6
	$\delta G_{\Phi\Phi\Lambda}$	−19.5	−16.9	−18.2
	$\delta G_{\Phi\Lambda H}$	−29.6	−18.0	−19.1
	$\delta G_{\Lambda\Lambda\Phi}$	−19.4	−15.1	−17.7
	$\delta G_{\Lambda\Lambda\Lambda}$	−20.1	−16.8	−17.7
	$\delta G_{HH\Phi}$	−19.6	−16.2	−17.5
	$\delta G_{HH\Lambda}$	−19.8	−16.9	−18.1
	δL_1	−20.1	−15.1	−17.2
	δL_2	−19.1	−16.4	−17.6
	δL_3	−18.9	−15.7	−17.0
20° × 20° in Fig. 8a	$\delta G_{\Phi\Phi\Phi}$	−28.4	−16.1	−17.3
	$\delta G_{\Phi\Phi\Lambda}$	−19.5	−16.3	−17.7
	$\delta G_{\Phi\Lambda H}$	−28.9	−16.9	−18.6
	$\delta G_{\Lambda\Lambda\Phi}$	−19.9	−15.0	−17.5
	$\delta G_{\Lambda\Lambda\Lambda}$	−19.0	−16.5	−17.3
	$\delta G_{HH\Phi}$	−18.9	−16.2	−17.4
	$\delta G_{HH\Lambda}$	−19.4	−16.8	−17.8
	δL_1	−19.0	−15.0	−17.0
	δL_2	−18.6	−16.2	−17.1
	δL_3	−19.0	−15.9	−16.9
10° × 10° in Fig. 8b	$\delta G_{\Phi\Phi\Phi}$	−26.6	−16.2	−17.0
	$\delta G_{\Phi\Phi\Lambda}$	−18.7	−15.8	−17.1
	$\delta G_{\Phi\Lambda H}$	−23.5	−16.6	−17.9
	$\delta G_{\Lambda\Lambda\Phi}$	−21.7	−14.9	−17.0
	$\delta G_{\Lambda\Lambda\Lambda}$	−18.6	−15.9	−16.6
	$\delta G_{HH\Phi}$	−19.6	−16.3	−17.1
	$\delta G_{HH\Lambda}$	−18.4	−15.8	−17.0
	δL_1	−18.9	−14.9	−16.6
	δL_2	−17.7	−15.4	−16.4
	δL_3	−18.5	−15.7	−16.6
5° × 5° in Fig. 8c	$\delta G_{\Phi\Phi\Phi}$	−26.5	−15.9	−16.7
	$\delta G_{\Phi\Phi\Lambda}$	−19.2	−15.5	−16.7
	$\delta G_{\Phi\Lambda H}$	−27.5	−15.8	−17.4
	$\delta G_{\Lambda\Lambda\Phi}$	−19.3	−14.9	−16.6
	$\delta G_{\Lambda\Lambda\Lambda}$	−18.0	−15.1	−16.2
	$\delta G_{HH\Phi}$	−19.2	−15.8	−16.6
	$\delta G_{HH\Lambda}$	−18.2	−15.7	−16.6
	δL_1	−19.1	−14.9	−16.2
	δL_2	−17.4	−15.1	−16.0
	δL_3	−19.7	−15.3	−16.1
1° × 1° in Fig. 8d	$\delta G_{\Phi\Phi\Phi}$	−21.6	−15.8	−16.6
	$\delta G_{\Phi\Phi\Lambda}$	−19.4	−15.2	−16.4
	$\delta G_{\Phi\Lambda H}$	−22.2	−15.8	−17.0
	$\delta G_{\Lambda\Lambda\Phi}$	−18.8	−14.9	−16.4
	$\delta G_{\Lambda\Lambda\Lambda}$	−19.2	−15.0	−16.3
	$\delta G_{HH\Phi}$	−18.6	−15.7	−16.5

Table 9 continued

Grid size	Quantity	Min	Max	Mean
	$\delta G_{HH\Lambda}$	−18.6	−15.3	−16.3
	δL_1	−18.2	−14.9	−16.0
	δL_2	−18.8	−14.8	−15.9
	δL_3	−18.2	−15.0	−16.0

Other parameters are the same as those in Table 4

is due to the interaction of the superposition error effect and the grid size refinement effect. A future study on this aspect will be investigated to reveal the interaction of two effects on the accuracy of evaluating gravitational quantities of the tesseroid.

The third-order central and single-sided finite difference formulas can be extended to the higher-order central and single-sided finite difference formulas based on Sects. 2.1–2.3. In addition, the numerical approach presented in Sect. 2.4 can be applied for evaluating higher-order gravitational potential gradients (Deng and Ran 2021). Regarding the numerical approach presented in this study, the constant to variable density with respect to the spherical latitudinal, longitudinal, and height directions of gravitational curvature will be studied based on Sect. 2.4 of Fukushima (2018). Although this study uses the homogeneous spherical shell as a benchmark to test the accuracy of the numerical approximations in Sect. 2, there still need complex mass bodies with analytical solutions for gravitational quantities to allow for more complex testing of the accuracy of the numerical approach (e.g., a spherical shell with arbitrary-order polynomial density in Deng (2023b)) and specific applications will need to be performed to reveal the actual accuracy of the numerical approach in practical scenarios.

Finally, the numerical approach to accurately calculate gravitational curvature of a tesseroid in this study can perform practical applications of gravitational curvature for the topographic effects, crustal effects, and other layers of arbitrary celestial bodies in geodesy, geophysics, and planetary sciences.

Appendix A Detailed expressions for the third-order partial derivatives in forms of numerical differentiation

Regarding the diagonal components of the third-order partial derivatives, the conditional switch of the $(\partial^3 V/\partial H^3)_{\Phi,\Lambda}$ can be obtained by:

(1) if $\Phi_S \le \Phi \le \Phi_N$ **and** $\Lambda_W \le \Lambda \le \Lambda_E$ **and** either $H_B < H < H_B + \Delta_3 H$ or $H_T < H < H_T + \Delta_3 H$, based on Eq. (13) by adopting $t = H$ with the positive sign, it yields:

$$\left(\frac{\partial^3 V}{\partial H^3}\right)_{\Phi,\Lambda} \approx \frac{1}{2(\Delta_3 H)^3}\big[-3V(\Phi,\Lambda,H+4\Delta_3 H) + 14V(\Phi,\Lambda,H+3\Delta_3 H) - 24V(\Phi,\Lambda,H+2\Delta_3 H) + 18V(\Phi,\Lambda,H+\Delta_3 H) - 5V(\Phi,\Lambda,H)\big] \quad \text{(A1)}$$

(2) else if $\Phi_S \le \Phi \le \Phi_N$ **and** $\Lambda_W \le \Lambda \le \Lambda_E$ **and** either $H_B - \Delta_3 H < H < H_B$ or $H_T - \Delta_3 H < H < H_T$, based on Eq. (13) by adopting $t = H$ with the negative sign, it yields:

$$\left(\frac{\partial^3 V}{\partial H^3}\right)_{\Phi,\Lambda} \approx \frac{1}{2(\Delta_3 H)^3}\big[3V(\Phi,\Lambda,H-4\Delta_3 H) - 14V(\Phi,\Lambda,H-3\Delta_3 H) + 24V(\Phi,\Lambda,H-2\Delta_3 H) - 18V(\Phi,\Lambda,H-\Delta_3 H) + 5V(\Phi,\Lambda,H)\big] \quad \text{(A2)}$$

(3) else, based on Eq. (3) by adopting $t = H$, it yields:

$$\left(\frac{\partial^3 V}{\partial H^3}\right)_{\Phi,\Lambda} \approx \frac{1}{2(\Delta_3 H)^3}\big[V(\Phi,\Lambda,H+2\Delta_3 H) - 2V(\Phi,\Lambda,H+\Delta_3 H) + 2V(\Phi,\Lambda,H-\Delta_3 H) - V(\Phi,\Lambda,H-2\Delta_3 H)\big] \quad \text{(A3)}$$

The other two diagonal components of the third-order partial derivatives (i.e., $(\partial^3 V/\partial \Phi^3)_{\Lambda,H}$ and $(\partial^3 V/\partial \Lambda^3)_{\Phi,H}$) can be analogously calculated by exchanging the roles between the H and Φ or Λ based on three situations of the $(\partial^3 V/\partial H^3)_{\Phi,\Lambda}$ in Eqs. (A1–A3).

Regarding the non-diagonal components with two variables of the third-order partial derivatives, the different conditional switches of the $[\partial^3 V/(\partial\Lambda\partial H^2)]_\Phi$ can be calculated by:

(1) if $\Phi_S \le \Phi \le \Phi_N$ **and** either $\Lambda_W < \Lambda < \Lambda_W + \Delta_3\Lambda$ or $\Lambda_E < \Lambda < \Lambda_E + \Delta_3\Lambda$ **and** either $H_B < H < H_B + \Delta_3 H$ or $H_T < H < H_T + \Delta_3 H$, then based on Eq. (18) by adopting $u = H$ and $v = \Lambda$ with two corresponding sign factors of $+1$ and $+1$, it yields:

$$\left(\frac{\partial^3 V}{\partial\Lambda\partial H^2}\right)_{\Phi} \approx \frac{1}{2(\Delta_3\Lambda)(\Delta_3 H)^2}\big[V(\Phi,\Lambda+2\Delta_3\Lambda,H+3\Delta_3 H) - 4V(\Phi,\Lambda+\Delta_3\Lambda,H+3\Delta_3 H)$$

$$
\begin{aligned}
&+3V(\Phi,\Lambda,H+3\Delta_3H)\\
&-4V(\Phi,\Lambda+2\Delta_3\Lambda,H+2\Delta_3H)\\
&+16V(\Phi,\Lambda+\Delta_3\Lambda,H+2\Delta_3H)\\
&-12V(\Phi,\Lambda,H+2\Delta_3H)\\
&+5V(\Phi,\Lambda+2\Delta_3\Lambda,H+\Delta_3H)\\
&-20V(\Phi,\Lambda+\Delta_3\Lambda,H+\Delta_3H)\\
&+15V(\Phi,\Lambda,H+\Delta_3H)\\
&-2V(\Phi,\Lambda+2\Delta_3\Lambda,H)\\
&+8V(\Phi,\Lambda+\Delta_3\Lambda,H)\\
&-6V(\Phi,\Lambda,H)\Big] \qquad \text{(A4)}
\end{aligned}
$$

(2) else if $\Phi_S \le \Phi \le \Phi_N$ **and** either $\Lambda_W - \Delta_3\Lambda < \Lambda < \Lambda_W$ or $\Lambda_E - \Delta_3\Lambda < \Lambda < \Lambda_E$ **and** either $H_B < H < H_B + \Delta_3 H$ or $H_T < H < H_T + \Delta_3 H$, then based on Eq. (18) by adopting $u = H$ and $v = \Lambda$ with two corresponding sign factors of $+1$ and -1, it yields:

$$
\begin{aligned}
\left(\frac{\partial^3 V}{\partial\Lambda\partial H^2}\right)_\Phi \approx \frac{-1}{2(\Delta_3\Lambda)(\Delta_3 H)^2}\Big[&\\
&V(\Phi,\Lambda-2\Delta_3\Lambda,H+3\Delta_3H)\\
&-4V(\Phi,\Lambda-\Delta_3\Lambda,H+3\Delta_3H)\\
&+3V(\Phi,\Lambda,H+3\Delta_3H)\\
&-4V(\Phi,\Lambda-2\Delta_3\Lambda,H+2\Delta_3H)\\
&+16V(\Phi,\Lambda-\Delta_3\Lambda,H+2\Delta_3H)\\
&-12V(\Phi,\Lambda,H+2\Delta_3H)\\
&+5V(\Phi,\Lambda-2\Delta_3\Lambda,H+\Delta_3H)\\
&-20V(\Phi,\Lambda-\Delta_3\Lambda,H+\Delta_3H)\\
&+15V(\Phi,\Lambda,H+\Delta_3H)\\
&-2V(\Phi,\Lambda-2\Delta_3\Lambda,H)\\
&+8V(\Phi,\Lambda-\Delta_3\Lambda,H)\\
&-6V(\Phi,\Lambda,H)\Big] \qquad \text{(A5)}
\end{aligned}
$$

(3) else if $\Phi_S \le \Phi \le \Phi_N$ **and** either $\Lambda_W < \Lambda < \Lambda_W + \Delta_3\Lambda$ or $\Lambda_E < \Lambda < \Lambda_E + \Delta_3\Lambda$ **and** either $H_B - \Delta_3 H < H < H_B$ or $H_T - \Delta_3 H < H < H_T$, then based on Eq. (18) by adopting $u = H$ and $v = \Lambda$ with two corresponding sign factors of -1 and $+1$, it yields:

$$
\begin{aligned}
\left(\frac{\partial^3 V}{\partial\Lambda\partial H^2}\right)_\Phi \approx \frac{1}{2(\Delta_3\Lambda)(\Delta_3 H)^2}\Big[&\\
&V(\Phi,\Lambda+2\Delta_3\Lambda,H-3\Delta_3H)\\
&-4V(\Phi,\Lambda+\Delta_3\Lambda,H-3\Delta_3H)\\
&+3V(\Phi,\Lambda,H-3\Delta_3H)\\
&-4V(\Phi,\Lambda+2\Delta_3\Lambda,H-2\Delta_3H)\\
&+16V(\Phi,\Lambda+\Delta_3\Lambda,H-2\Delta_3H)\\
&-12V(\Phi,\Lambda,H-2\Delta_3H)\\
&+5V(\Phi,\Lambda+2\Delta_3\Lambda,H-\Delta_3H)\\
&-20V(\Phi,\Lambda+\Delta_3\Lambda,H-\Delta_3H)\\
&+15V(\Phi,\Lambda,H-\Delta_3H)\\
&-2V(\Phi,\Lambda+2\Delta_3\Lambda,H)\\
&+8V(\Phi,\Lambda+\Delta_3\Lambda,H)\\
&-6V(\Phi,\Lambda,H)\Big] \qquad \text{(A6)}
\end{aligned}
$$

(4) else if $\Phi_S \le \Phi \le \Phi_N$ **and** either $\Lambda_W - \Delta_3\Lambda < \Lambda < \Lambda_W$ or $\Lambda_E - \Delta_3\Lambda < \Lambda < \Lambda_E$ **and** either $H_B - \Delta_3 H < H < H_B$ or $H_T - \Delta_3 H < H < H_T$, then based on Eq. (18) by adopting $u = H$ and $v = \Lambda$ with two corresponding sign factors of -1 and -1, it yields:

$$
\begin{aligned}
\left(\frac{\partial^3 V}{\partial\Lambda\partial H^2}\right)_\Phi \approx \frac{-1}{2(\Delta_3\Lambda)(\Delta_3 H)^2}\Big[&\\
&V(\Phi,\Lambda-2\Delta_3\Lambda,H-3\Delta_3H)\\
&-4V(\Phi,\Lambda-\Delta_3\Lambda,H-3\Delta_3H)\\
&+3V(\Phi,\Lambda,H-3\Delta_3H)\\
&-4V(\Phi,\Lambda-2\Delta_3\Lambda,H-2\Delta_3H)\\
&+16V(\Phi,\Lambda-\Delta_3\Lambda,H-2\Delta_3H)\\
&-12V(\Phi,\Lambda,H-2\Delta_3H)\\
&+5V(\Phi,\Lambda-2\Delta_3\Lambda,H-\Delta_3H)\\
&-20V(\Phi,\Lambda-\Delta_3\Lambda,H-\Delta_3H)\\
&+15V(\Phi,\Lambda,H-\Delta_3H)\\
&-2V(\Phi,\Lambda-2\Delta_3\Lambda,H)\\
&+8V(\Phi,\Lambda-\Delta_3\Lambda,H)\\
&-6V(\Phi,\Lambda,H)\Big] \qquad \text{(A7)}
\end{aligned}
$$

(5) else if $\Phi_S \le \Phi \le \Phi_N$ **and** either $\Lambda < \Lambda_W - \Delta_3\Lambda$ or $\Lambda_W + \Delta_3\Lambda < \Lambda < \Lambda_E - \Delta_3\Lambda$ or $\Lambda_E + \Delta_3\Lambda < \Lambda$ **and** either $H_B < H < H_B + \Delta_3 H$ or $H_T < H < H_T + \Delta_3 H$, then based on Eq. (17) by adopting $u = H$ and $v = \Lambda$ with the positive sign for $u = H$, it yields:

$$
\begin{aligned}
\left(\frac{\partial^3 V}{\partial\Lambda\partial H^2}\right)_\Phi \approx \frac{1}{2(\Delta_3\Lambda)(\Delta_3 H)^2}\Big[&\\
&-V(\Phi,\Lambda+\Delta_3\Lambda,H+3\Delta_3H)\\
&+V(\Phi,\Lambda-\Delta_3\Lambda,H+3\Delta_3H)\\
&+4V(\Phi,\Lambda+\Delta_3\Lambda,H+2\Delta_3H)\\
&-4V(\Phi,\Lambda-\Delta_3\Lambda,H+2\Delta_3H)\\
&-5V(\Phi,\Lambda+\Delta_3\Lambda,H+\Delta_3H)\\
&+5V(\Phi,\Lambda-\Delta_3\Lambda,H+\Delta_3H)\\
&+2V(\Phi,\Lambda+\Delta_3\Lambda,H)\\
&-2V(\Phi,\Lambda-\Delta_3\Lambda,H)\Big] \qquad \text{(A8)}
\end{aligned}
$$

(6) else if $\Phi_S \le \Phi \le \Phi_N$ **and** either $\Lambda < \Lambda_W - \Delta_3\Lambda$ or $\Lambda_W + \Delta_3\Lambda < \Lambda < \Lambda_E - \Delta_3\Lambda$ or $\Lambda_E + \Delta_3\Lambda < \Lambda$ **and**

either $H_B-\Delta_3 H < H < H_B$ or $H_T-\Delta_3 H < H < H_T$, then based on Eq. (17) by adopting $u = H$ and $v = \Lambda$ with the negative sign for $u = H$, it yields:

$$\left(\frac{\partial^3 V}{\partial\Lambda\partial H^2}\right)_\Phi \approx \frac{1}{2(\Delta_3\Lambda)(\Delta_3 H)^2}\big[- V(\Phi, \Lambda+\Delta_3\Lambda, H-3\Delta_3 H) + V(\Phi, \Lambda-\Delta_3\Lambda, H-3\Delta_3 H) + 4V(\Phi, \Lambda+\Delta_3\Lambda, H-2\Delta_3 H) - 4V(\Phi, \Lambda-\Delta_3\Lambda, H-2\Delta_3 H) - 5V(\Phi, \Lambda+\Delta_3\Lambda, H-\Delta_3 H) + 5V(\Phi, \Lambda-\Delta_3\Lambda, H-\Delta_3 H) + 2V(\Phi, \Lambda+\Delta_3\Lambda, H) - 2V(\Phi, \Lambda-\Delta_3\Lambda, H)\big] \quad \text{(A9)}$$

(7) else if $\Phi_S \le \Phi \le \Phi_N$ **and** either $\Lambda_W < \Lambda < \Lambda_W + \Delta_3\Lambda$ or $\Lambda_E < \Lambda < \Lambda_E + \Delta_3\Lambda$ **and** either $H < H_B - \Delta_3 H$ or $H_B+\Delta_3 H < H < H_T-\Delta_3 H$ or $H_T+\Delta_3 H < H$, then based on Eq. (16) by adopting $u = H$ and $v = \Lambda$ with the positive sign for $v = \Lambda$, it yields:

$$\left(\frac{\partial^3 V}{\partial\Lambda\partial H^2}\right)_\Phi \approx \frac{1}{2(\Delta_3\Lambda)(\Delta_3 H)^2}\big[- V(\Phi, \Lambda+2\Delta_3\Lambda, H+\Delta_3 H) + 4V(\Phi, \Lambda+\Delta_3\Lambda, H+\Delta_3 H) - 3V(\Phi, \Lambda, H+\Delta_3 H) + 2V(\Phi, \Lambda+2\Delta_3\Lambda, H) - 8V(\Phi, \Lambda+\Delta_3\Lambda, H) + 6V(\Phi, \Lambda, H) - V(\Phi, \Lambda+2\Delta_3\Lambda, H-\Delta_3 H) + 4V(\Phi, \Lambda+\Delta_3\Lambda, H-\Delta_3 H) - 3V(\Phi, \Lambda, H-\Delta_3 H)\big] \quad \text{(A10)}$$

(8) else if $\Phi_S \le \Phi \le \Phi_N$ **and** either $\Lambda_W - \Delta_3\Lambda < \Lambda < \Lambda_W$ or $\Lambda_E - \Delta_3\Lambda < \Lambda < \Lambda_E$ **and** either $H < H_B - \Delta_3 H$ or $H_B+\Delta_3 H < H < H_T-\Delta_3 H$ or $H_T+\Delta_3 H < H$, then based on Eq. (16) by adopting $u = H$ and $v = \Lambda$ with the negative sign for $v = \Lambda$, it yields:

$$\left(\frac{\partial^3 V}{\partial\Lambda\partial H^2}\right)_\Phi \approx \frac{-1}{2(\Delta_3\Lambda)(\Delta_3 H)^2}\big[- V(\Phi, \Lambda-2\Delta_3\Lambda, H+\Delta_3 H) + 4V(\Phi, \Lambda-\Delta_3\Lambda, H+\Delta_3 H) - 3V(\Phi, \Lambda, H+\Delta_3 H) + 2V(\Phi, \Lambda-2\Delta_3\Lambda, H) - 8V(\Phi, \Lambda-\Delta_3\Lambda, H) + 6V(\Phi, \Lambda, H) - V(\Phi, \Lambda-2\Delta_3\Lambda, H-\Delta_3 H) + 4V(\Phi, \Lambda-\Delta_3\Lambda, H-\Delta_3 H) - 3V(\Phi, \Lambda, H-\Delta_3 H)\big] \quad \text{(A11)}$$

(9) else, based on Eq. (15) by adopting $u = H$ and $v = \Lambda$, it yields:

$$\left(\frac{\partial^3 V}{\partial\Lambda\partial H^2}\right)_\Phi \approx \frac{1}{2(\Delta_3\Lambda)(\Delta_3 H)^2}\big[V(\Phi, \Lambda+\Delta_3\Lambda, H+\Delta_3 H) - V(\Phi, \Lambda-\Delta_3\Lambda, H+\Delta_3 H) - 2V(\Phi, \Lambda+\Delta_3\Lambda, H) + 2V(\Phi, \Lambda-\Delta_3\Lambda, H) + V(\Phi, \Lambda+\Delta_3\Lambda, H-\Delta_3 H) - V(\Phi, \Lambda-\Delta_3\Lambda, H-\Delta_3 H)\big] \quad \text{(A12)}$$

The other five non-diagonal components with two variables of the third-order partial derivatives (i.e., $[\partial^3 V/(\partial\Phi^2\partial\Lambda)]_H$, $[\partial^3 V/(\partial\Phi^2\partial H)]_\Lambda$, $[\partial^3 V/(\partial\Phi\partial\Lambda^2)]_H$, $[\partial^3 V/(\partial\Lambda^2\partial H)]_\Phi$, and $[\partial^3 V/(\partial\Phi\partial H^2)]_\Lambda$) can similarly be obtained by exchanging the roles among the Φ, Λ, and H based on nine situations of the $[\partial^3 V/(\partial\Lambda\partial H^2)]_\Phi$ in Eqs. (A4–A12).

Regarding the non-diagonal components with three variables of the third-order partial derivatives, different twenty-seven conditional switches of the $\partial^3 V/(\partial\Phi\partial\Lambda\partial H)$ can be obtained by applying the positive and negative signs in Eqs. (19–22) based on three situations of the $(\partial^3 V/\partial H^3)_{\Phi,\Lambda}$ in Eqs. (A1–A3) and nine situations of the $[\partial^3 V/(\partial\Lambda\partial H^2)]_\Phi$ in Eqs. (A4–A12). Specifically, there are one conditional switch for Eq. (19), six (i.e., $3\times 2 = 6$) conditional switches for Eq. (20), twelve (i.e., $3\times 2\times 2 = 12$) conditional switches for Eq. (21), and eight (i.e., $2\times 2\times 2 = 8$) conditional switches for Eq. (22).

To make related expressions more clear, the expressions for other third-order partial derivatives ($(\partial^3 V/\partial\Phi^3)_{\Lambda,H}$, $(\partial^3 V/\partial\Lambda^3)_{\Phi,H}$, $[\partial^3 V/(\partial\Phi^2\partial\Lambda)]_H$, $[\partial^3 V/(\partial\Phi^2\partial H)]_\Lambda$, $[\partial^3 V/(\partial\Phi\partial\Lambda^2)]_H$, $[\partial^3 V/(\partial\Lambda^2\partial H)]_\Phi$, $[\partial^3 V/(\partial\Phi\partial H^2)]_\Lambda$, and $\partial^3 V/(\partial\Phi\partial\Lambda\partial H)$) are presented in the *Expressions-for-other-third-order-partial-derivatives.pdf* at https://github.com/xiaoledeng/xtessgc-xqtessgc.

Appendix B Validation of the derived expressions for gravitational curvature of a tesseroid

The nine expressions for gravitational curvature components in Eqs. (35–37) and (39–44) can be validated using Laplace's

equation as:

$$G_{\Phi\Phi\Phi} + G_{\Lambda\Lambda\Phi} + G_{HH\Phi} = 0 \tag{B13}$$

$$G_{\Phi\Phi\Lambda} + G_{\Lambda\Lambda\Lambda} + G_{HH\Lambda} = 0 \tag{B14}$$

$$G_{\Phi\Phi H} + G_{\Lambda\Lambda H} + G_{HHH} = 0 \tag{B15}$$

If three sums in Eqs. (B13–B15) are all equal to zero after substituting nine expressions in Eqs. (35–37) and (39–44), the correctness of nine gravitational curvature expressions can be confirmed.

The main step is substituting the expressions for the third-order partial derivatives, gravitational vector, and gravitational gradient tensor of a tesseroid in spherical coordinates into Eqs. (35–37) and (39–44). The expressions for gravitational vector and gravitational gradient tensor are presented in Eqs. (24) and (28–33) of Fukushima (2018) (see also Eqs. (3–4) of Deng (2023a)). The first-, second-, and third-order derivatives of gravitational potential can be obtained by taking the partial derivatives of gravitational potential with respect to the spherical coordinates (Φ, Λ, H) of the computation point. The Newton integral for gravitational potential (V) of a tesseroid in spherical coordinates was presented as:

$$V = G\rho \int_{\Phi_S}^{\Phi_N} \int_{\Lambda_W}^{\Lambda_E} \int_{R_1}^{R_2} \frac{R'^2 \cos\Phi'}{l} \mathrm{d}R' \mathrm{d}\Lambda' \mathrm{d}\Phi' \tag{B16}$$

$$l = \sqrt{R^2 + R'^2 - 2RR'[\sin\Phi \sin\Phi' + \cos\Phi \cos\Phi' \cos(\Lambda - \Lambda')]} \tag{B17}$$

$$R = R_0 + H, \quad R' = R_0 + H' \tag{B18}$$

$$R_1 = R_0 + H_B, \quad R_2 = R_0 + H_T \tag{B19}$$

where ρ is the density of the tesseroid. $[\Lambda_W, \Lambda_E]$, $[\Phi_S, \Phi_N]$, and $[H_B, H_T]$ (or $[R_1, R_2]$) are the boundaries of the tesseroid along the directions of the longitude, latitude, and height (or geocentric distance). (Φ, Λ, H) and (Φ', Λ', H') are the spherical Gauss normal coordinates with latitudes, longitudes, and heights of the computation and integration points. l is the distance between the computation and integration points. R and R' are the geocentric distances of the computation and integration points.

To reveal the detailed process, the Mathematica code (*Appendix1.nb*) is provided at https://github.com/xiaoledeng/xtessgc-xqtessgc. After running all codes in *Appendix1.nb*, three sums in Eqs. (B13–B15) are all equal to zero, which confirms the correctness of nine gravitational curvature expressions in Eqs. (35–37) and (39–44). $G_{\Phi\Lambda H}$ in Eq. (38) is not analytically validated because it is not involved in Laplace's equation for gravitational curvature in Eqs. (B13–B15).

Appendix C: Computer codes

Based on the Fortran codes `xtess.f90` and `xqtess.f90` to calculate gravitational potential, gravitational vector, and gravitational gradient tensor of a tesseroid (Fukushima 2018; Deng 2023a) at https://github.com/xiaoledeng/xtess-xqtess, the Fortran codes `xtessgc.f90` and `xqtessgc.f90` to calculate gravitational curvature of a tesseroid are presented at https://github.com/xiaoledeng/xtessgc-xqtessgc.

Under the same computer hardware (i.e., Intel i5-10400 CPU at 2.9 GHz using the single-threaded operation) and numerical settings in Sect. 4 of Deng (2023a), the total computation time of the `xtessgc.f90` and `xqtessgc.f90` to compute gravitational potential, gravitational vector, gravitational gradient tensor, and gravitational curvature is approximately 11.750 / 40 ≈ 0.294 s and 167.150 s precomputation point with a single tesseroid in double and quadruple precision, respectively.

When calculating gravitational curvature of a tesseroid in practical applications with `xtessgc.f90` and `xqtessgc.f90`, one should additionally multiply the term $G\rho R_0^2$ with the numerical results of gravitational curvature to acquire the unit $\mathrm{m}^{-1}\,\mathrm{s}^{-2}$ for gravitational curvature, in which the units of the G, ρ, and R_0 are $\mathrm{m}^3\,\mathrm{kg}^{-1}\,\mathrm{s}^{-2}$, $\mathrm{kg}\,\mathrm{m}^{-3}$, and m, respectively.

Herein, the main Fortran subroutines and functions to calculate gravitational potential, gravitational vector, gravitational gradient tensor, and gravitational curvature ($G_{\Phi\Phi\Phi}$, $G_{\Phi\Phi\Lambda}$, $G_{\Phi\Phi H}$, $G_{\Phi\Lambda H}$, $G_{\Lambda\Lambda\Phi}$, $G_{\Lambda\Lambda\Lambda}$, $G_{\Lambda\Lambda H}$, $G_{HH\Phi}$, $G_{HH\Lambda}$, and G_{HHH}) of a tesseroid in quadruple precision are illustrated in Fig. 9.

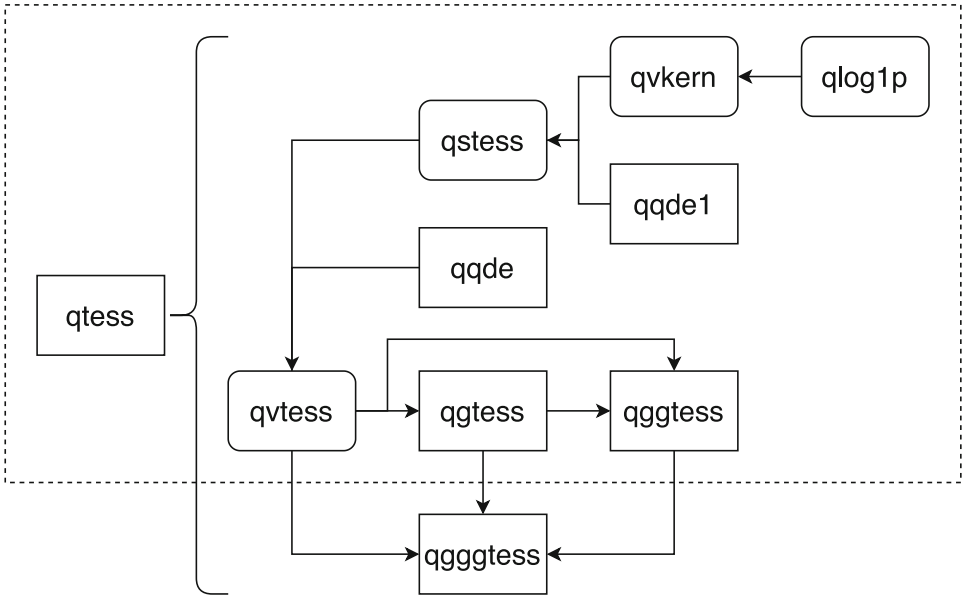

Fig. 9 Illustration of the main Fortran subroutines (i.e. **qtess**, **qgtess**, **qggtess**, **qgggtess**, **qqde**, and **qqde1**) and functions (i.e., **qvtess**, **qstess**, **qvkern**, and **qlog1p**) to calculate gravitational potential (**qvtess**), gravitational vector (**qgtess**), gravitational gradient tensor (**qggtess**), and gravitational curvature (**qgggtess**) of a tesseroid in quadruple precision. The subroutines and functions in the dashed box are from `xqtess.f90` (Fukushima 2018; Deng 2023a). The subroutine **qgggtess** to calculate gravitational curvature is from Sect. 2.4 in this study. **qtess** is the main subroutine to calculate gravitational potential, gravitational vector, gravitational gradient tensor, and gravitational curvature of a tesseroid. **qvtess** is the function to integrate gravitational potential as $V(\Phi, \Lambda, H) = \int_{\xi_S}^{\xi_N} Q(\xi)\mathrm{d}\xi$ with $\xi_S = \Phi_S - \Phi$ and $\xi_N = \Phi_N - \Phi$ using the conditional split quadrature of the latitude line integration from Eq. (1) in Electronic Supplementary Materials of Fukushima (2018). **qstess** is the function to calculate $Q(\xi) = \int_{\eta_W}^{\eta_E} P(\eta)\mathrm{d}\eta$ with $\eta_W = \Lambda_W - \Lambda$ and $\eta_E = \Lambda_E - \Lambda$ using the conditional split quadrature of the longitude line integration from Eq. (2) in Electronic Supplementary Materials of Fukushima (2018). **qvkern** is the function to evaluate the kernel function $P(\eta)$ in cancelation-free form with the unit $G\rho = 1$ from Eq. (13) and Appendix A of Fukushima (2018). **qqde1** is the complete copy subroutine of the **qqde** to integrate $s = \int_a^b f(x)\mathrm{d}x$ using the double exponential rule (Takahasi and Mori 1973, 1974; Mori 1985; Fukushima 2017, 2018) with the relative error tolerance δ_0 from Appendix B of Fukushima (2018). **qlog1p** is the function to calculate the $\ln(1 + x)$ function using the minimax approximation with a type (13, 13) rational function based on Appendix D of Fukushima (2017)

Acknowledgements We are grateful to Editor-in-Chief P. Xu, Editor P. Novák, and three anonymous reviewers for their valuable comments, which helped improve the manuscript.

Funding Open Access funding enabled and organized by Projekt DEAL. This study is supported by the German Research Foundation (DFG, Deutsche Forschungsgemeinschaft) under project number 549821068.

Data Availability The Fortran codes to calculate gravitational curvature of a tesseroid in double and quadruple precision are openly available at https://github.com/xiaoledeng/xtessgc-xqtessgc.

Declarations

Conflict of interest The author declares no competing financial interests.

References

Casotto S, Fantino E (2009) Gravitational gradients by tensor analysis with application to spherical coordinates. J Geod 83(7):621–634. https://doi.org/10.1007/s00190-008-0276-z

Deng XL (2023a) Corrections to: "Accurate computation of gravitational field of a tesseroid" by Fukushima (2018) in J. Geod. 92(12):1371–1386. J Geod 97(1):8. https://doi.org/10.1007/s00190-022-01673-2

Deng XL (2023b) Evaluation of gravitational curvatures for a tesseroid and spherical shell with arbitrary-order polynomial density. J Geod 97(2):18. https://doi.org/10.1007/s00190-023-01708-2

Deng XL, Ran J (2021) Higher-order gravitational potential gradients by tensor analysis in spherical coordinates. J Geod 95(7):1–13. https://doi.org/10.1007/s00190-021-01539-z

Deng XL, Shen WB (2018a) Evaluation of gravitational curvatures of a tesseroid in spherical integral kernels. J Geod 92(4):415–429. https://doi.org/10.1007/s00190-017-1073-3

Deng XL, Shen WB (2018b) Evaluation of optimal formulas for gravitational tensors up to gravitational curvatures of a tesseroid. Surv Geophys 39(3):365–399. https://doi.org/10.1007/s10712-018-9460-8

Deng XL, Shen WB (2019) Topographic effects up to gravitational curvatures of tesseroids: A case study in China. Stud Geophys Geod 63(3):345–366. https://doi.org/10.1007/s11200-018-0772-4

Deng XL, Sneeuw N (2023) Analytical solutions for gravitational potential up to its third-order derivatives of a tesseroid, spherical zonal band, and spherical shell. Surv Geophys 44(4):1125–1173. https://doi.org/10.1007/s10712-023-09774-z

Du J, Qiu F (2019) Third-order gradient tensor of gravitational potential and preliminary analysis of its exploration capacity. J Geod Geodyn 39(4):331–338. https://doi.org/10.14075/j.jgg.2019.04.001. (in Chinese)

Fukushima T (2017) Precise and fast computation of the gravitational field of a general finite body and its application to the gravitational study of asteroid Eros. Astron J 154(4):145. https://doi.org/10.3847/1538-3881/aa88b8

Fukushima T (2018) Accurate computation of gravitational field of a tesseroid. J Geod 92(12):1371–1386. https://doi.org/10.1007/s00190-018-1126-2

Ghobadi-Far K, Sharifi MA, Sneeuw N (2016) 2D Fourier series representation of gravitational functionals in spherical coordinates. J Geod 90(9):871–881. https://doi.org/10.1007/s00190-016-0916-7

Hamáčková E, Šprlák M, Pitoňák M, Novák P (2016) Non-singular expressions for the spherical harmonic synthesis of gravitational curvatures in a local north-oriented reference frame. Comput Geosci 88:152–162. https://doi.org/10.1016/j.cageo.2015.12.011

Mori M (1985) Quadrature formulas obtained by variable transformation and the DE-rule. J Comput Appl Math 12–13:119–130. https://doi.org/10.1016/0377-0427(85)90011-1

Nagy D, Papp G, Benedek J (2000) The gravitational potential and its derivatives for the prism. J Geod 74(7–8):552–560. https://doi.org/10.1007/s001900000116

Novák P, Šprlák M, Tenzer R, Pitonák M (2017) Integral formulas for transformation of potential field parameters in geosciences. Earth-Sci Rev 164:208–231. https://doi.org/10.1016/j.earscirev.2016.10.007

Novák P, Pitoňák M, Šprlák M, Tenzer R (2019) Higher-order gravitational potential gradients for geoscientific applications. Earth-Sci Rev 198(102):937. https://doi.org/10.1016/j.earscirev.2019.102937

Novák P, Šprlák M, Pitoňák M (2021) On determination of the geoid from measured gradients of the Earth's gravity field potential. Earth-Sci Rev 221(103):773. https://doi.org/10.1016/j.earscirev.2021.103773

Ouyang F, Chen LW, Wu L (2024) 3D large-scale forward modeling of gravitational fields using triangular spherical prisms with polynomial densities in depth. J Geod 98(6):53. https://doi.org/10.1007/s00190-024-01863-0

Pitoňák M, Eshagh M, Šprlák M , Tenzer R, Novák P (2018) Spectral combination of spherical gravitational curvature boundary-value problems. Geophys J Int 214(2):773–791. https://doi.org/10.1093/gji/ggy147

Pitoňák M, Novák P, Eshagh M , Tenzer R, Sprlák M (2020) Downward continuation of gravitational field quantities to an irregular surface by spectral weighting. J Geod 94(7):62. https://doi.org/10.1007/s00190-020-01384-6

Qiu F, Du J, Chen C (2019) Forward modeling formulae for third-order gradient tensor of gravitational potential caused by the right rectangular prism. J Geod Geodyn 39(3):313–316. https://doi.org/10.14075/j.jgg.2019.03.018. (in Chinese)

Romeshkani M, Sharifi MA, Tsoulis D (2019) Joint estimation of gravity anomalies using second and third order potential derivatives. Geophys J Int 220(2):1197–1207. https://doi.org/10.1093/gji/ggz517

Romeshkani M, Sharifi MA, Tsoulis D (2021) Estimation of gravitational curvature through a deterministic approach and spectral combination of space-borne second-order gravitational potential derivatives. Geophys J Int 224(2):825–842. https://doi.org/10.1093/gji/ggaa466

Rosi G, Cacciapuoti L, Sorrentino F, Menchetti M, Prevedelli M, Tino GM (2015) Measurement of the gravity-field curvature by atom interferometry. Phys Rev Lett 114(1). https://doi.org/10.1103/physrevlett.114.013001

Rummel R, Yi W, Stummer C (2011) GOCE gravitational gradiometry. J Geod 85(11):777–790. https://doi.org/10.1007/s00190-011-0500-0

Šprlák M, Novák P (2015) Integral formulas for computing a third-order gravitational tensor from volumetric mass density, disturbing gravitational potential, gravity anomaly and gravity disturbance. J Geod 89(2):141–157. https://doi.org/10.1007/s00190-014-0767-z

Šprlák M, Novák P (2016) Spherical gravitational curvature boundary-value problem. J Geod 90(8):727–739. https://doi.org/10.1007/s00190-016-0905-x

Šprlák M, Novák P (2017) Spherical integral transforms of second-order gravitational tensor components onto third-order gravitational tensor components. J Geod 91(2):167–194. https://doi.org/10.1007/s00190-016-0951-4

Šprlák M, Pitoňák M (2024a) Far-zone effects for spherical integral transformations I: Formulas for the radial boundary value problem and its derivatives. Surv Geophys 45(3):977–1009. https://doi.org/10.1007/s10712-023-09818-4

Šprlák M, Pitoňák M (2024b) Far-zone effects for spherical integral transformations II: Formulas for horizontal boundary value problems and their derivatives. Surv Geophys 45(5):1663–1713. https://doi.org/10.1007/s10712-024-09842-y

Šprlák M, Novák P, Pitoňák M (2016) Spherical harmonic analysis of gravitational curvatures and its implications for future satellite missions. Surv Geophys 37(3):681–700. https://doi.org/10.1007/s10712-016-9368-0

Takahasi H, Mori M (1973) Quadrature formulas obtained by variable transformation. Numer Math 21(3):206–219. https://doi.org/10.1007/bf01436624

Takahasi H, Mori M (1974) Double exponential formulas for numerical integration. Publ Res Inst Math Sci 9(3):721–741. https://doi.org/10.2977/prims/1195192451